Wideband Power Amplifier Modeling Incorporating Carrier Frequency Dependent AM/AM and AM/PM Characteristics

Andre Tkacenko*

In this article, we present a complex baseband model for a wideband power amplifier that incorporates carrier frequency dependent amplitude modulation (AM) and phase modulation (PM) (i.e., AM/AM and AM/PM) characteristics in the design process. The structure used to implement the amplifier model is a Wiener system which accounts for memory effects caused by the frequency selective nature of the amplifier, in addition to the nonlinearities caused by gain compression and saturation. By utilizing piecewise polynomial nonlinearities in the structure, it is shown how to construct the Wiener model to exactly accommodate all given AM/AM and AM/PM measurement constraints. Simulation results using data from a 50 W 32-way Ka-band solid state power amplifier (SSPA) are provided, highlighting the differences in degradation incurred for a wideband input signal as compared with a narrowband input.

I. Introduction

With the ever increasing desire to raise data rates for satellite and deep space communications has come the interest to analyze power amplifier effects on wideband telemetry type signals. One such amplifier of particular interest at JPL is a 50 W Ka-band solid state power amplifier (SSPA) [1, 2] constructed from 32 monolithic microwave integrated circuit (MMIC) [3] modules. This amplifier, which we will refer to here as the 50 W 32-way Ka-band SSPA, is intended for use in future spacecraft missions for wideband telemetry. In addition to accounting for nonlinearities of amplifiers such as the 32-way SSPA due to gain compression and saturation [3], analysis for wideband input signals must also account for the carrier frequency varying nature inherent to these

*Communications Architectures and Research Section

The research described in this publication was carried out by the Jet Propulsion Laboratory, California Institute of Technology, under a contract with the National Aeronautics and Space Administration. © 2013 California Institute of Technology. U. S. Government sponsorship acknowledged.

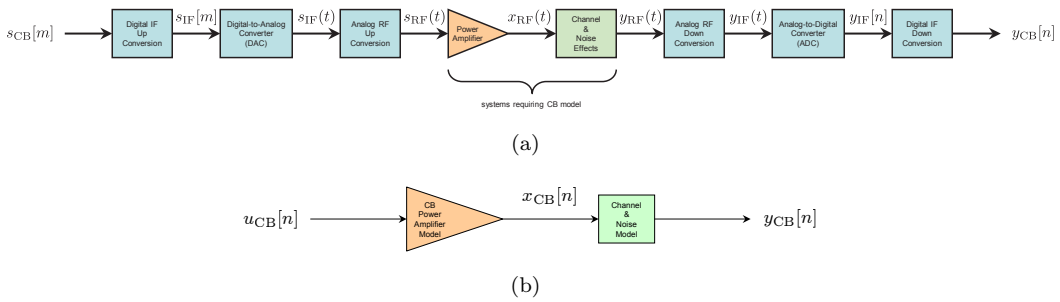

Figure 1. Transmitter/receiver digital telemetry block diagrams: (a) the general IF/RF up/down conversion setup and (b) a simplified CB equivalent.

amplifiers. This frequency dependent behavior is commonly attributed to memory effects present in these amplifiers due to stray capacitances as well as other passive elements [4].

In order to assess digital telemetry performance degradations caused by a given nonlinear power amplifier, it is useful to develop a discrete-time complex baseband (CB) model for the amplifier. To that end, it is fruitful to first chart the development of such a digital telemetry signal as it progresses from the transmitter to the receiver. A digital telemetry signal generally undergoes intermediate frequency (IF) as well as radio frequency (RF) up/down conversion [5] as shown in the block diagram of Fig. 1(a). By lumping together the various operations of IF/RF up/down conversion along with digital-to-analog and analog-to-digital conversion, the IF/RF system shown in Fig. 1(a) can be replaced with the simplified CB block diagram system of Fig. 1(b). Here, the discrete-time signal $u_{CB}[n]$ represents an oversampled version of the continuous-time signal $s_{CB}(t)$ corresponding to the discrete-time signal $s_{CB}[m]$ [6, 7]. In other words, $u_{CB}[n]$ is an interpolated version of the original CB input signal $s_{CB}[m]$ from Fig. 1(a). Typically, the sample rate corresponding to $u_{CB}[n]$ is an integer multiple of the data symbol rate corresponding to $s_{CB}[m]$.

Several attempts have been made to characterize wideband nonlinear amplifiers in the literature (see Sec. II for a survey of some of the most popular methods). The challenge in developing a useful model comes as a result of the fact that there is no exact method for characterizing a nonlinear system, as opposed to a linear system which can be completely characterized by impulse responses known as Green's functions [6, 7]. Because of this, the development of a nonlinear power amplifier model is usually broken down into three primary stages. First, an analytical model is *postulated*. Afterwards, the parameters of such a model must be *identified* using given information about the amplifier. Finally, the model can be deemed satisfactory once it is *validated* against actual data recovered from the amplifier for realistic input signals.

There is usually very little data available to characterize a given nonlinear power amplifier. Typically, an amplifier is characterized according to its response to a continuous wave (CW) input [4]. Specifically, an amplitude modulation (AM) of the CW input causes modulation of the amplitude as well as phase modulation (PM) of the output. (It is nearly

always assumed that PM of the input has no effect on the output [4]). This leads to an AM/AM and AM/PM characteristic for the amplifier [4]. (Typically, input/output amplitudes are given in relative dB (dBr) [4], whereas output phase shifts are given in degrees (deg).) Based on these two characteristic functions, a memoryless model for the CB amplifier system shown in Fig. 1(b) given below is often used:

$$x_{\mathrm{CB}}[n] = 10^{\frac{P\left(10\log_{10}\left(|u_{\mathrm{CB}}[n]|^2\right)\right)}{20}} e^{j\left(\arg(u_{\mathrm{CB}}[n]) + \frac{\pi}{180}\phi\left(10\log_{10}\left(|u_{\mathrm{CB}}[n]|^2\right)\right)\right)}. \tag{1}$$

Here, $P(v)$ is the AM/AM function (with input and output in dBr), whereas $\phi(v)$ is the AM/PM function (with input in dBr and output in deg). Though rudimentary, the memoryless nonlinear amplifier input/output relationship of (1) is typically a good model for narrowband input signals.

For the 50 W 32-way Ka-band SSPA, the only available data to characterize the amplifier model consists of AM/AM and AM/PM measurements taken across 61 different carrier frequencies uniformly distributed between 30.0-36.0 GHz. Since these characteristics vary with carrier frequency, the memoryless model of (1) is unable to capture all of the effects of the amplifier for wideband input signals. As such, a more sophisticated analytical model is required here.

In this article, we focus on a special type of analytical model known as a Wiener nonlinear system [8, 9] to accommodate carrier frequency dependent AM/AM and AM/PM characteristics. Using an advance/delay based Wiener system with piecewise polynomial memoryless nonlinearities (see Sec. IV), we show by construction how to exactly satisfy all AM/AM and AM/PM measurement constraints. Applying the data from the 50 W 32-way Ka-band SSPA, we then provide simulation results to illustrate the different degradations obtained for wideband signals as opposed to narrowband inputs. It is observed that the presence of frequency selectivity in the amplifier has a deleterious effect on wideband input signals when compared with analogous narrowband inputs, in line with intuition.

A. Outline

In Sec. II, we present a brief survey of previous literature pertaining to wideband power amplifier modeling, including the three-box model (Sec. II-A), Wiener/Hammerstein systems (Sec. II-B), and Volterra series expansion approaches (Sec. II-C). Afterwards, in Sec. III, we introduce the notion of carrier frequency dependent AM/AM and AM/PM characteristics. There, we show how such characteristics are mapped to the complex baseband domain and ultimately incorporated into the modeling process. In Sec. IV, we introduce the advance/delay based Wiener system with piecewise polynomial nonlinearities and show how such a system can be parameterized to exactly match a given set of AM/AM and AM/PM constraints. Specifically, the parameterization is carried out for three distinct power regions; a low power linear region (Sec. IV-A), a mid power AM/AM and AM/PM characteristic region (Sec. IV-B), and a high power saturation region (Sec. IV-C). Implementation details related to generating a so-called universal input drive level axis as required for the Wiener system are presented in Sec. IV-D. In Sec. V, we

present various simulation results for the proposed Wiener system model using data from the 50 W 32-way Ka-band SSPA, including noise power ratio (NPR) simulations (Sec. V-A), telemetry sample density and spectral regrowth results (Sec. V-B), error vector magnitude (EVM) and out-of-band power simulations (Sec. V-C), and bit error rate (BER) results (Sec. V-D). There, the different amplifier degradations incurred for a wideband input signal with respect to a narrowband input are shown. Finally, concluding remarks are made in Sec. VI.

B. Notations

All notations used are as in [6, 7]. In particular, continuous-time (analog) and discrete-time (digital) normalized frequencies are denoted by F and f, respectively. Parentheses and square brackets are respectively used for continuous-time and discrete-time function arguments. For example, $x(t)$ would denote a continuous-time function for $t \in \mathbb{R}$, whereas $y[n]$ would denote a discrete-time function for $n \in \mathbb{Z}$. Boldface lowercase letters (such as $\mathbf{v}$) are used to denote vectors, whereas boldface uppercase letters (such as $\mathbf{A}$) are used to denote matrices.

Here, the letter z is reserved as the z-transform [6, 7] variable, whereas v is reserved as the input variable of a generally nonlinear system operator. Thus, in block diagram figures, $H(z)$ would denote a linear time invariant (LTI) filter [6, 7] corresponding to the z-transform $H(z)$, whereas $F(v)$ would denote a generally nonlinear system with input v and output $F(v)$.

In line with standard notation, decibels are abbreviated as dB, whereas milliwatts (mW) in dB are abbreviated dBm. Here, dBr is used to denote relative dB [4], which are decibels measured with respect to some reference power level (usually 1 mW or 1 W). Specifically, dBr is used for sake of generality when deriving the wideband amplifier model of Sec. IV.

II. Survey of Wideband Power Amplifier Modeling Techniques

In this section, we explore some of the previous approaches in the literature that have been made to develop a wideband CB nonlinear amplifier model. Given the difficulty inherent to modeling nonlinearities in general [4], it is not surprising that several different models have been proposed, each with its own merits and faults. In addition to these diverse approaches, the data available from the amplifiers used to characterize the wideband models typically varies as well from author to author. Though here, we will parameterize our wideband model solely from the carrier frequency dependent AM/AM and AM/PM measurements, several authors use the amplifier output to a select signal type such as a telemetry waveform to construct their respective models [9, 10, 11]. In this case, the model is typically parameterized to minimize the mean squared error between the actual amplifier and model outputs.

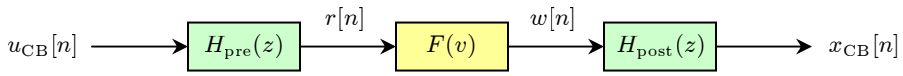

Figure 2. Three-box model block diagram.

A. Three-Box Model

One of the first attempts at developing a frequency dependent model of an amplifier came from Saleh's landmark paper concerning an analytical model for traveling wave tube amplifiers (TWTAs) [12]. In this article, a *three-box model* was proposed to characterize the frequency dependent behavior of an amplifier. This three-box model consisted of a linear pre-filter, followed by a memoryless nonlinearity, followed by a linear post-filter, as shown in Fig. 2.

In a typical amplifier model of this type [4, 13], the pre-filter $H_{\mathrm{pre}}(z)$ is chosen as the *small signal gain response* [4] of the amplifier, whereas the memoryless nonlinearity $F(v)$ is chosen as a single AM/AM and AM/PM type nonlinearity as in (1). The post-filter $H_{\mathrm{post}}(z)$ in many applications is bypassed altogether (leading to a two-box model), but can be chosen to optimally shape the output power spectrum [13].

Though the three-box model is simple to implement in practice and can lead to a satisfactory model of an amplifier, it does not hold for wideband amplifiers in which the AM/AM and AM/PM curve shapes change with carrier frequency, such as the 50 W 32-way Ka-band SSPA (see Sec. III). The reason for this is that the AM/AM and AM/PM curves for each frequency are simply horizontal and vertical translations of the AM/AM and AM/PM curves defined by the nonlinearity $F(v)$ [14]. To see this, suppose that, similar to (1), the input/output relationship of the memoryless nonlinearity $F(v)$ from Fig. 2 is as follows:

$$F(v) = 10^{\frac{P_{\mathrm{out}}\left(10\log_{10}\left(|v|^2\right)\right)}{20}} e^{j\left(\arg(v)+\frac{\pi}{180}\phi_{\mathrm{out}}\left(10\log_{10}\left(|v|^2\right)\right)\right)}. \tag{2}$$

Here, $P_{\mathrm{out}}(v)$ and $\phi_{\mathrm{out}}(v)$ denote the AM/AM and AM/PM functions, respectively. Suppose that the input $u_{\mathrm{CB}}[n]$ is chosen as a CW tone (similar to the input used to obtain AM/AM and AM/PM measurements in general) of the following form:

$$u_{\mathrm{CB}}[n] \triangleq 10^{\frac{P_{\mathrm{in}}}{20}} e^{j2\pi f_{\mathrm{in}} n}. \tag{3}$$

Here, P_{in} denotes the input power in dBr and f_{in} denotes the discrete-time frequency of the CW input (which maps to a particular carrier frequency as discussed in Sec. III). From Fig. 2, the output of the pre-filter $H_{\mathrm{pre}}(z)$, namely $r[n]$, is as follows [6, 7]:

$$r[n] = \left(10^{\frac{P_{\mathrm{in}}}{20}} e^{j2\pi f_{\mathrm{in}} n}\right) H_{\mathrm{pre}}\left(e^{j2\pi f_{\mathrm{in}}}\right) = 10^{\frac{P_{\mathrm{in}}+10\log_{10}\left(\left|H_{\mathrm{pre}}\left(e^{j2\pi f_{\mathrm{in}}}\right)\right|^2\right)}{20}} e^{j\left(2\pi f_{\mathrm{in}} n+\arg\left(H_{\mathrm{pre}}\left(e^{j2\pi f_{\mathrm{in}}}\right)\right)\right)}.$$

Continuing further, it can be shown from (2) that the output of the nonlinearity $F(v)$, namely $w[n]$, is given by the following expression:

$$\begin{aligned} w[n] \;=\; & 10^{\frac{P_{\mathrm{out}}\left(P_{\mathrm{in}}+10\log_{10}\left(\left|H_{\mathrm{pre}}\left(e^{j2\pi f_{\mathrm{in}}}\right)\right|^2\right)\right)}{20}} \\ & \times e^{j\left(2\pi f_{\mathrm{in}} n+\arg\left(H_{\mathrm{pre}}\left(e^{j2\pi f_{\mathrm{in}}}\right)\right)+\frac{\pi}{180}\phi_{\mathrm{out}}\left(P_{\mathrm{in}}+10\log_{10}\left(\left|H_{\mathrm{pre}}\left(e^{j2\pi f_{\mathrm{in}}}\right)\right|^2\right)\right)\right)}. \end{aligned}$$

Finally, from this, it can be shown that the output of the post-filter $H_{\text{post}}(z)$, namely $x_{\text{CB}}[n]$, is as follows:

$$x_{\text{CB}}[n] = 10^{\frac{P_{\text{out}}\left(P_{\text{in}}+10\log_{10}\left(\left|H_{\text{pre}}\left(e^{j2\pi f_{\text{in}}}\right)\right|^2\right)\right)+10\log_{10}\left(\left|H_{\text{post}}\left(e^{j2\pi f_{\text{in}}}\right)\right|^2\right)}{20}} \times e^{j\left(2\pi f_{\text{in}} n+\frac{\pi}{180}\left(\phi_{\text{out}}\left(P_{\text{in}}+10\log_{10}\left(\left|H_{\text{pre}}\left(e^{j2\pi f_{\text{in}}}\right)\right|^2\right)\right)+\frac{180}{\pi}\left(\arg\left(H_{\text{pre}}\left(e^{j2\pi f_{\text{in}}}\right)\right)+\arg\left(H_{\text{post}}\left(e^{j2\pi f_{\text{in}}}\right)\right)\right)\right)\right)}. \tag{4}$$

Comparing (3) and (4), it is clear that a CW input leads to a CW output at the same tone frequency. Also, the output amplitude and phase shift are dictated by the input power as well as parameters related to the pre/post-filters $H_{\text{pre}}(z)$ and $H_{\text{post}}(z)$. This leads to *frequency dependent* AM/AM and AM/PM characteristics. If $P_{\text{out};f_{\text{in}}}(v)$ and $\phi_{\text{out};f_{\text{in}}}(v)$ denote, respectively, the AM/AM and AM/PM characteristic functions corresponding to the input frequency f_{in}, then we have the following from (4):

$$\begin{aligned} P_{\text{out};f_{\text{in}}}(P_{\text{in}}) &= P_{\text{out}}\Bigg(P_{\text{in}}+\underbrace{10\log_{10}\left(\left|H_{\text{pre}}\left(e^{j2\pi f_{\text{in}}}\right)\right|^2\right)}_{\text{vertical shift}}\Bigg)+\underbrace{10\log_{10}\left(\left|H_{\text{post}}\left(e^{j2\pi f_{\text{in}}}\right)\right|^2\right)}_{\text{horizontal shift}}, \\ \phi_{\text{out};f_{\text{in}}}(P_{\text{in}}) &= \phi_{\text{out}}\Bigg(P_{\text{in}}+\underbrace{10\log_{10}\left(\left|H_{\text{pre}}\left(e^{j2\pi f_{\text{in}}}\right)\right|^2\right)}_{\text{vertical shift}}\Bigg) \\ &\quad +\underbrace{\frac{180}{\pi}\left(\arg\left(H_{\text{pre}}\left(e^{j2\pi f_{\text{in}}}\right)\right)+\arg\left(H_{\text{post}}\left(e^{j2\pi f_{\text{in}}}\right)\right)\right)}_{\text{horizontal shift}}. \end{aligned} \tag{5}$$

As can be seen from (5), the frequency dependent AM/AM and AM/PM curves are obtained by horizontal and vertical translations of the given AM/AM and AM/PM curves, respectively. Here, the magnitude response of the pre-filter $H_{\text{pre}}(z)$ adjusts the vertical shift of both the AM/AM and AM/PM curves, whereas the magnitude response of the post-filter $H_{\text{post}}(z)$ sets the horizontal shift of the AM/AM curve. Similarly, the phase responses of both filters set the horizontal shift of the AM/PM curve, as is evident from (5). Thus, the AM/AM and AM/PM curves at all frequencies are of the same *shape*.

As mentioned above, the measured AM/AM and AM/PM characteristics for the 50 W 32-way Ka-band SSPA are of different shapes for different frequencies. Specifically, the AM/PM characteristics vary significantly in shape as a function of carrier frequency (see Sec. III). Hence, the three-box model of Fig. 2 is not a sufficient system to emulate the behavior of this amplifier and so a more sophisticated model is in order.

B. Wiener/Hammerstein Systems

One advantageous feature of the three-box model is that it decouples memory effects from the nonlinearities. Specifically, the memory effects are handled by the linear filters, whereas the nonlinearities are addressed in a memoryless fashion. This can simplify the model parameterization process, as evidenced by the frequency dependent AM/AM and AM/PM curves of (5).

One way to promote the notion of decoupling memory effects with nonlinearities is to

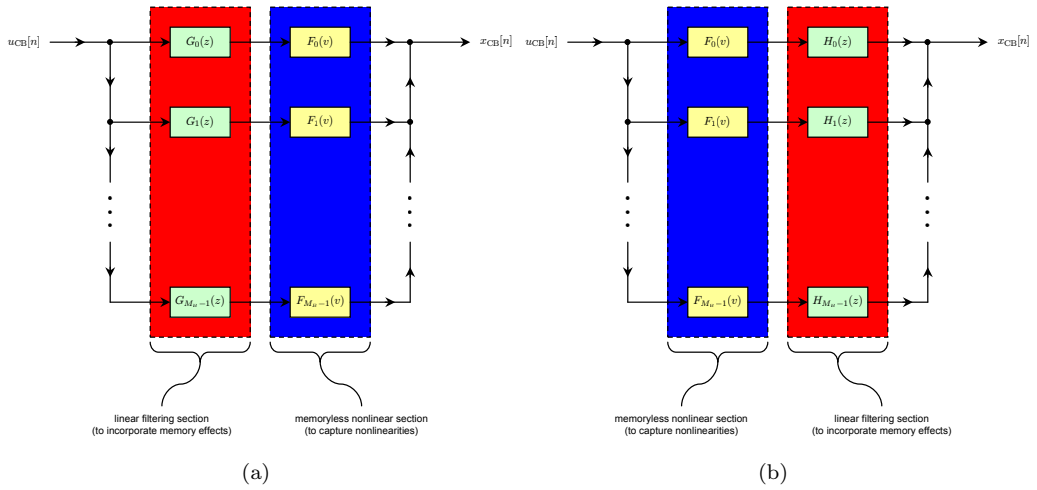

Figure 3. Multi-branch decoupled memory/nonlinearity system block diagrams: (a) the Wiener system and (b) the Hammerstein system.

combine branches of such decoupled systems. A multi-branch *Wiener* nonlinear system [8, 9] consists of a set of linear filtering operations followed by memoryless nonlinearities. Similarly, a multi-branch *Hammerstein* nonlinear system [15, 11] is the dual to the Wiener system and consists of a set of memoryless nonlinearities followed by linear filtering operations. These are illustrated in Fig. 3 for (a) a Wiener system and (b) a Hammerstein system. Here, M_B denotes the number of branches used in each system.

Wiener systems have served as a popular model for wideband amplifiers in the literature. For example, in [8], a Wiener system was designed based on two-tone intermodulation distortion (IMD) [14] measurements. Also, in [9], a Wiener system was parameterized to best fit (in a least squares sense) an actual amplifier output and the model output. Simulations for an IS-95B telemetry signal [4] showed good agreement between the Wiener model and actual amplifier output for a particular RF laterally diffused metal-oxide semiconductor (LDMOS) power amplifier (PA). In [10], the authors considered a similar type of Wiener system as those from [9], but considered piecewise polynomial spline functions [16] for the nonlinearities instead of regular polynomials.

Hammerstein systems have likewise been popularly considered in the literature. For example, in [11], a Hammerstein system was parameterized to fit an actual amplifier output and model output in a least squares sense. Simulation results for a wideband code division multiple access (WCDMA) [5] input to an LDMOS PA showed good agreement in terms of spectral regrowth [4]. Also, in [15], a Hammerstein system was designed based on frequency dependent AM/AM and AM/PM characteristics. This system approximated the desired AM/AM and AM/PM characteristics in a least squares sense and was shown to validate well against actual amplifier output samples for a discrete multi-tone (DMT) [4] telemetry signal.

Of all of the Wiener and Hammerstein systems mentioned here, one that showed particular

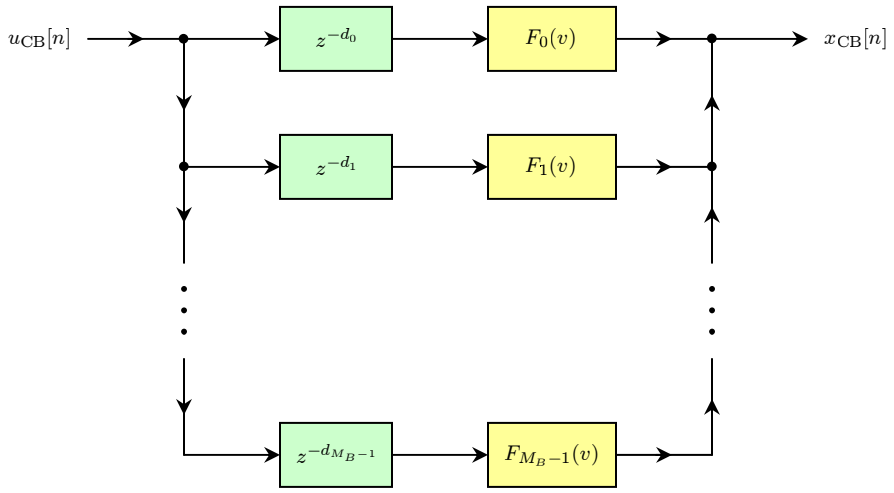

Figure 4. Memory polynomial model with sparse delay taps (MPMSD) block diagram. (Special type of Wiener nonlinear system.)

promise was the memory polynomial model with sparse delay taps (MPMSD) system of [9]. This model is a special type of Wiener nonlinear system and is shown in Fig. 4. In [9], the memoryless nonlinearities $\{F_k(v)\}_{0\le k\le M_B-1}$ were polynomials of the following form:

$$F_k(v) = \sum_{m=1}^{M} a_{2m-1,k}\,|v|^{2(m-1)}\,v\,,\ 0 \le k \le M_B - 1\,. \tag{6}$$

Hence, the MPMSD system was completely characterized by the set of delays values $\{d_k\}_{0\le k\le M_B-1}$ and polynomial coefficients $\{a_{2m-1,k}\}_{1\le m\le M,0\le k\le M_B-1}$. For a given set of delays, the coefficients were chosen to minimize the mean squared error between the model output and a test vector of actual amplifier output samples. Then, the delays were varied exhaustively over a certain range to obtain the best possible fit. Simulation results from independent authors [17] showed the superiority of the MPMSD system to a more general Volterra based system in terms of spectral regrowth for a WCDMA input to an LDMOS PA.

The performance of the MPMSD, coupled with its ease of parameterization, have served as the impetus for its use here for frequency dependent AM/AM and AM/PM characteristics. This, however, involves replacing the polynomial nonlinearities of (6) with a more sophisticated function, as discussed in Sec. IV.

Note that the Wiener and Hammerstein models of Fig. 3 can be combined to obtain a more general nonlinear system. Such a joint Wiener/Hammerstein model is shown in Fig. 5. Here, each branch consists of a linear pre-filtering section followed by a memoryless nonlinearity followed in turn by a linear post-filtering section. From Figs. 2 and 5, it is clear that the three-box model is simply a special case of this Wiener/Hammerstein model for $M_B = 1$.

Prior to proceeding further, a final comment is in order regarding the wideband amplifier

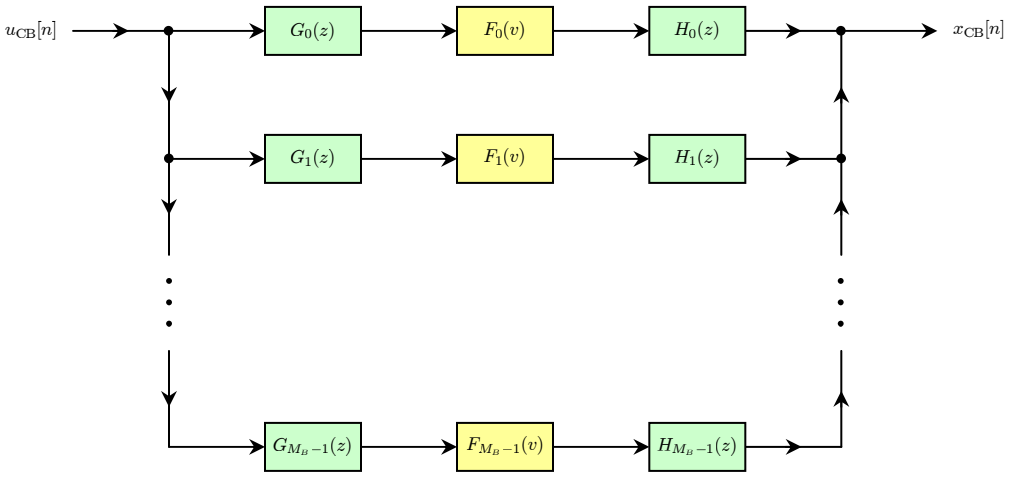

Figure 5. Multi-branch Wiener/Hammerstein system block diagram.

design problem here. From Fig. 3(a), it can be seen that the Wiener nonlinear system can be easily configured to conform to a set of frequency dependent AM/AM and AM/PM characteristics. For example, if there are N_f frequencies, then by choosing $M_B = N_f$, the filters $\{G_k(z)\}_{0\leq k\leq M_B-1}$ to allow only one such frequency to pass, and setting the nonlinearities $\{F_k(v)\}_{0\leq k\leq M_B-1}$ to the given AM/AM and AM/PM characteristics for each frequency, then the overall system will indeed satisfy all of the desired properties. However, the linear filtering operations will tend to suppress IMD present between different tones in a multi-tonal input. This phenomenon will not occur for the MPMSD type of system from Fig. 4, since the filtering operations are delays and hence are allpass [6, 7]. It is for this reason that we have opted use the MPMSD system as the basis for our proposed wideband model here. As will be shown in Sec. IV, such a system can chosen to *exactly* satisfy all given AM/AM and AM/PM measurement constraints.

C. Volterra Series Expansion Approaches

Thus far, we have only discussed systems in which memory effects were decoupled from nonlinear phenomena. A more general system, however, takes such interrelations into account. One such system is that based on a *Volterra* series expansion [18], which is a generalization of a Taylor series expansion [5] for systems with memory.

In general, a system with input $u_{\mathrm{CB}}[n]$ and output $x_{\mathrm{CB}}[n]$ has the following Volterra series expansion [18, 19]:

$$x_{\mathrm{CB}}[n] = \sum_{k=1}^{\infty}\left[\sum_{m_1=-\infty}^{\infty}\sum_{m_2=-\infty}^{\infty}\cdots\sum_{m_k=-\infty}^{\infty} h_k\left[m_1, m_2, \ldots, m_k\right]\left(\prod_{\ell=1}^{k} u_{\mathrm{CB}}\left[n-m_\ell\right]\right)\right]. \quad (7)$$

Here, the sequences $\{h_k\left[m_1, m_2, \ldots, m_k\right]\}$ are called *kernels* of the Volterra series expansion [18].

Though the input/output model of (7) mixes memory effects with nonlinearities, it is

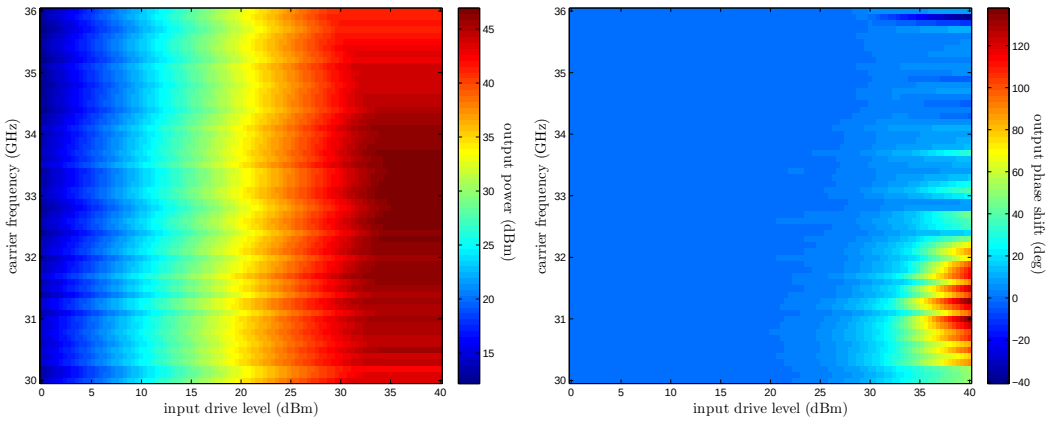

Figure 6. Image plots of measurement data for the 50 W 32-way Ka-band SSPA: (a) AM/AM characteristics and (b) AM/PM characteristics.

difficult to emulate in a practical setting. One reason for this is that the kernels are difficult to extract from the given data [19]. Another reason is that many kernels are required to obtain a suitable approximation to the complete series expansion of (7) [20].

Volterra based systems with mixed memory effects and nonlinearities have been considered in the literature. In [20], a system based on a pruned complex variant of the series expansion of (7) was considered and modeled using actual amplifier output samples. Simulation results showed a close match between the actual amplifier and model output samples. In [19], a Volterra series projected onto orthonormal Laguerre functions was considered and modeled for a set of actual amplifier output samples. As with [20], simulations yielded good agreement between the model and amplifier outputs.

Due to the difficulties inherent with deriving a successful Volterra based model, we have opted here to instead focus on the more simplistic MPMSD Wiener system of Fig. 4.

III. Incorporating Carrier Frequency Dependent AM/AM and AM/PM Measurements in the Modeling Process

Recall from Sec. I that for the 50 W 32-way Ka-band SSPA, the only data available to characterize the amplifier consists of AM/AM and AM/PM measurements taken across 61 different carrier frequencies uniformly distributed between 30.0-36.0 GHz. An image plot of the AM/AM and AM/PM characteristics is shown in Fig. 6(a) and (b), respectively, for the different carrier frequencies. For an alternate view of these measurements, a surface plot of these respective characteristics is also shown in Fig. 7. It should be noted that here, the delay due to the amplifier was removed, leading to the zero phase shift condition that can be observed in the AM/PM characteristics at the lowest input drive level value.

As can be seen from the plots, the amplifier characteristics indeed vary considerably with

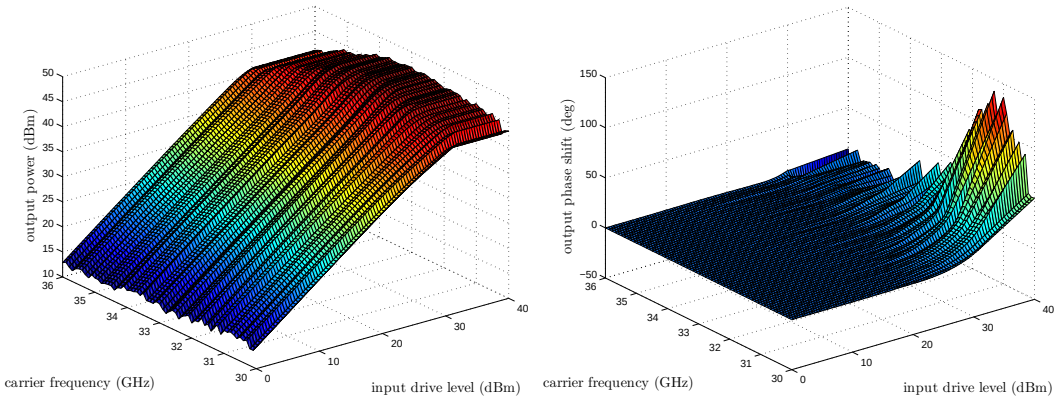

(a) (b)

Figure 7. Surface plots of measurement data for the 50 W 32-way Ka-band SSPA: (a) AM/AM characteristics and (b) AM/PM characteristics.

carrier frequency. From the AM/AM measurements, it can be seen that the frequency selectivity of the amplifier is evident, as is the gain compression and saturation at large input drives. Furthermore, from the AM/PM measurements, it can be observed that the phase shift due to the amplifier appears to grow linearly with input drive for large input drive levels and that the phase shift varies considerably with carrier frequency, especially near 31 GHz.

With such carrier frequency dependent behavior, one question that arises is that of how to map the RF related constraints to the CB domain. Specifically, for the CB amplifier model of Fig. 1(b), the question is how the analog RF constraints from the AM/AM and AM/PM measurements translate to the digital CB domain. To answer this question, consider a wideband input signal whose analog RF spectrum is shown in Fig. 8(a). Here, F_c and $F_{\rm BW}$ denote the analog carrier frequency and bandwidth of the wideband input signal, respectively. Also, $F_{c,k}$ denotes the k-th carrier frequency value from the AM/AM and AM/PM measurements for $0 \leq k \leq N_F - 1$, where N_F denotes the number of carrier frequency measurement values. For the 32-way SSPA, we have $N_F = 61$, $F_{c,0} = 30.0$ GHz and $F_{c,0} = 36.0$ GHz. Note that for a fixed bandwidth of $F_{\rm BW}$, the carrier frequency of the wideband signal F_c must satisfy $F_{c,0} + \frac{F_{\rm BW}}{2} \leq F_c \leq F_{c,N_F-1} - \frac{F_{\rm BW}}{2}$.

Implicit in the CB model of Fig. 1(b) is the sampling rate used at the ADC of Fig. 1(a). If this sampling rate is F_s, where we assume $F_s > F_{\rm BW}$ here, then the digital CB spectrum of the sampled signal is as shown in Fig. 8(b). Here, the digital bandwidth of the sampled wideband input signal $f_{\rm BW}$ is given by $f_{\rm BW} = \frac{F_{\rm BW}}{F_s}$. Under the RF down conversion and sampling mapping, the k-th carrier frequency from the AM/AM and AM/PM measurements (i.e., $F_{c,k}$) gets mapped to the following digital frequency number ν_k:

$$\nu_k \triangleq \frac{F_{c,k} - F_c}{F_s}\,,\ 0 \leq k \leq N_F - 1\,. \tag{8}$$

It should be noted that as a result of the sampling process, not all of the digital frequency

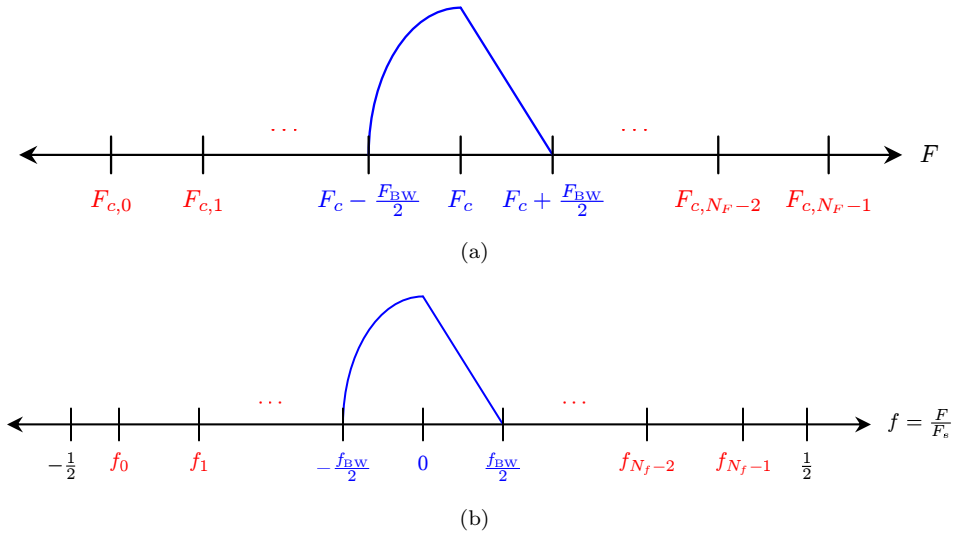

Figure 8. Spectra of a wideband input signal: (a) the original analog RF spectrum and (b) the sampled digital CB spectrum.

numbers ν_k from (8) will map to the digital CB spectrum domain [6, 7]. Specifically, only those k such that $-\frac{1}{2} \leq \nu_k < \frac{1}{2}$ will be mapped. Suppose that k_0 is the smallest index value of k such that $\nu_k \geq -\frac{1}{2}$ and that a total of N_f frequencies get mapped. Then, only the numbers $f_q \triangleq \nu_{k_0+q}$ for $0 \leq q \leq N_f - 1$ get mapped to the digital CB spectrum domain as shown in Fig. 8(b). Note that of these N_f frequencies, several could lie within the digital bandwidth of the input signal (i.e., within $-\frac{f_{\mathrm{BW}}}{2} \leq f < \frac{f_{\mathrm{BW}}}{2}$), depending on the value of the analog bandwidth value F_{BW}. This will lead to frequency selective behavior of the amplifier as will be shown in Sec. V through simulations.

With this analysis, we are now ready to stipulate the AM/AM and AM/PM constraints that we would like enforced by a wideband CB amplifier model such as the one from Fig. 1(b). Typically, AM/AM and AM/PM measurements are carried out over a discrete and finite set of input drive levels and carrier frequencies. For each carrier frequency appearing in the sampled CB spectrum f_q with $0 \leq q \leq N_f - 1$, there will be in general N_{P_q} points over which the AM/AM and AM/PM measurements will be defined. Hence, the set of AM/AM and AM/PM measurements to be satisfied here is as follows:

$$\begin{aligned} \{P_{\mathrm{in}}[p_q, q], P_{\mathrm{out}}[p_q, q]\}_{0 \leq p_q \leq N_{P_q}-1, 0 \leq q \leq N_f-1} \quad &- \quad \text{set of AM/AM measurements}, \\ \{P_{\mathrm{in}}[p_q, q], \vartheta[p_q, q]\}_{0 \leq p_q \leq N_{P_q}-1, 0 \leq q \leq N_f-1} \quad &- \quad \text{set of AM/PM measurements}. \end{aligned} \tag{9}$$

Here, P_{in} denotes the input drive level (in dBr), P_{out} denotes the output power (also in dBr), and ϑ denotes the output phase shift (in deg).

Recall that the AM/AM and AM/PM characteristics are derived as the response of an amplifier to a CW tone input signal [4]. Specifically, a CW input is assumed to be output by the amplifier as another CW signal with an amplitude correction and phase shift dictated by the AM/AM and AM/PM characteristics [4]. With this, the set of AM/AM

and AM/PM measurements from (9) leads to the following input/output constraints:

$$\begin{aligned} \text{Input}: \quad & u_{p_q,q}[n] = 10^{\frac{P_{\text{in}}[p_q,q]}{20}} e^{j2\pi f_q n} \\ \text{Output}: \quad & x_{p_q,q}[n] = 10^{\frac{P_{\text{out}}[p_q,q]}{20}} e^{j\left(2\pi f_q n + \frac{\pi}{180}\vartheta[p_q,q]\right)} \end{aligned} \quad , \; 0 \le p_q \le N_{P_q} - 1, 0 \le q \le N_f - 1 \, . \tag{10}$$

Here, we would like any wideband amplifier designed here to satisfy the input/output relationship of (10). In Sec. IV, we show how to construct a special Wiener nonlinear system (specifically an advance/delay based Wiener system with piecewise polynomial nonlinearities) to satisfy the constraints of (10) *exactly*. Furthermore, we show how to configure this model to satisfy additional low and high power constraints.

IV. Piecewise Polynomial Wiener Model for Frequency Dependent AM/AM and AM/PM Measurements

Prior to introducing the analytical model we will use to enforce the AM/AM and AM/PM constraints, it is imperative to mention the only restriction that we have here. Instead of the general AM/AM and AM/PM set of measurements from (9), we stipulate that all AM/AM and AM/PM measurements be defined over the same set of input drive levels across the carrier frequencies. This set of input drive levels will be called the *universal input drive level axis* and will serve as the set of knots [16] of the piecewise polynomial functions to be introduced below. As we discuss later on in Sec. IV-D, this restriction can still allow all of the original AM/AM and AM/PM measurement constraints from (9) to be satisfied by the analytical model here by defining additional constraints over a universal input drive level axis.

Let $\{\mathcal{P}_{\text{in}}[0], \mathcal{P}_{\text{in}}[1], \ldots, \mathcal{P}_{\text{in}}[N_P - 1]\}$ denote the set of universal input drive level axis values, where we assume $\mathcal{P}_{\text{in}}[0] < \mathcal{P}_{\text{in}}[1] < \cdots < \mathcal{P}_{\text{in}}[N_P - 1]$ and N_P denotes the number of input drive level power values. We assume here that our AM/AM and AM/PM measurement constraints are now of the following form:

$$\begin{aligned} \{\mathcal{P}_{\text{in}}[p], \mathcal{P}_{\text{out}}[p,q]\}_{0 \le p \le N_P - 1, 0 \le q \le N_f - 1} \quad & - \quad \text{set of AM/AM measurements}\,, \\ \{\mathcal{P}_{\text{in}}[p], \theta[p,q]\}_{0 \le p \le N_P - 1, 0 \le q \le N_f - 1} \quad & - \quad \text{set of AM/PM measurements}\,. \end{aligned} \tag{11}$$

Here, $\mathcal{P}_{\text{in}}$ denotes the input drive level (in dBr), $\mathcal{P}_{\text{out}}$ denotes the output power (also in dBr), and θ denotes the output phase shift (in deg).

The analytical model that we will use here will be similar to the MPMSD system of Fig. 4. One of the differences here will be that instead of choosing the memoryless nonlinearity

$F_k(v)$ as the polynomial based function of (6), we will use the following piecewise function:

$$F_k(v) = \begin{cases} h_k v\,, & \mathcal{P} < \mathcal{P}_{\text{in}}[0] \\ \left(10^{\frac{\widehat{\mathcal{P}}_k(\mathcal{P})}{20}} e^{j\left(\frac{\pi}{180}\widehat{\theta}_k(\mathcal{P})\right)}\right) e^{j\arg(v)}\,, & \mathcal{P}_{\text{in}}[0] \le \mathcal{P} \le \mathcal{P}_{\text{in}}[N_P-1] \\ \left(\sum_{\ell=0}^{N_f-1} K_{k,\ell} e^{j\left(\frac{\pi}{180}\alpha_\ell \mathcal{P}\right)}\right) e^{j\arg(v)}\,, & \mathcal{P} > \mathcal{P}_{\text{in}}[N_P-1] \end{cases}, \; \mathcal{P} \triangleq 10\log_{10}\left(|v|^2\right). \tag{12}$$

Here, $\{h_k\}_{0\le k\le M_B-1}$ denotes a set of low power linear region weights. Also, $\left\{\widehat{\mathcal{P}}_k(v)\right\}_{0\le k\le M_B-1}$ and $\left\{\widehat{\theta}_k(v)\right\}_{0\le k\le M_B-1}$ denote a respective set of mid power range output power and output phase shift piecewise polynomials of order M_P [7] with

$$\widehat{\mathcal{P}}_k(v) = \sum_{m=0}^{M_P-1} \widehat{p}_{k,m}(v) v^m\,,\; \widehat{\theta}_k(v) = \sum_{m=0}^{M_P-1} \widehat{\phi}_{k,m}(v) v^m\,,\; \text{knots at } \{\mathcal{P}_{\text{in}}[0]\,, \mathcal{P}_{\text{in}}[1]\,, \ldots, \mathcal{P}_{\text{in}}[N_P-1]\}\,. \tag{13}$$

Finally, $\{K_{k,\ell}\}_{0\le k\le M_B-1, 0\le \ell\le N_f-1}$ denotes a set of high power saturation region coefficients, whereas $\{\alpha_\ell\}_{0\le \ell\le N_f-1}$ denotes a set of linear phase values for the phase in the saturation region, determined by a linear least squares fit of the AM/PM curves in the high power region. Note that $F_k(v)$ as in (12) is piecewise with respect to the instantaneous power $\mathcal{P} = 10\log_{10}\left(|v|^2\right)$.

Since $\{\alpha_\ell\}_{0\le \ell\le N_f-1}$ is solely a function of the AM/PM characteristics and can be precomputed, the parameter set completely characterizing the analytical model is as follows:

$$\left\{\{h_k\}_{0\le k\le M_B-1}\,, \left\{\widehat{\mathcal{P}}_k(v)\right\}_{0\le k\le M_B-1}\,, \left\{\widehat{\theta}_k(v)\right\}_{0\le k\le M_B-1}\,, \{K_{k,\ell}\}_{0\le k\le M_B-1, 0\le \ell\le N_f-1}\right\}. \tag{14}$$

As we will soon show, by proper choice of the parameters from (14), the model of Fig. 4 with the memoryless nonlinearities of (12) will not only satisfy the desired AM/AM and AM/PM constraints of (11), but will also satisfy additional low power linear region and high power saturation region conditions.

In all of the simulations presented in Sec. V, we take the number of branches M_B in Fig. 4 to be odd and choose the delays d_k for $0 \le k \le M_B - 1$ as follows:

$$d_k = k - \left(\frac{M_B-1}{2}\right),\; 0 \le k \le M_B - 1\,. \tag{15}$$

As this choice makes approximately half of the delays negative, we will refer to the analytical model that we will use here as the advance/delay based Wiener system with piecewise polynomial memoryless nonlinearities. Though d_k will be chosen as in (15) for the simulations, the theoretical analysis below will be carried out for the general case of d_k.

A. Low Power Linear Region Modeling

For low powers (i.e., $\mathcal{P} < \mathcal{P}_{\text{in}}[0]$), we would like the amplifier to be completely linear. The choice of $F_k(v)$ as in (12) definitely ensures this. To obtain the linear weights

$\{h_k\}_{0\le k\le M_B-1}$, we choose them to satisfy the following linearity constraints for the CW tone inputs from which the AM/AM and AM/PM measurements were derived.

Low power linear region constraints: ($\mathcal{P} < \mathcal{P}_{\text{in}}[0]$)

$$\begin{aligned} \text{Input}: \quad & u_q[n] = 10^{\frac{\mathcal{P}}{20}} e^{j2\pi f_q n} \\ \text{Output}: \quad & x_q[n] = \left(10^{\frac{\mathcal{P}_{\text{out}}[0,q]-\mathcal{P}_{\text{in}}[0]}{20}} e^{j\left(\frac{\pi}{180}\theta[0,q]\right)}\right) \cdot 10^{\frac{\mathcal{P}}{20}} e^{j2\pi f_q n} \end{aligned} \quad , \ \forall\ \mathcal{P} < \mathcal{P}_{\text{in}}[0]\,,\ 0 \le q \le N_f - 1\,. \tag{16}$$

Let $\widehat{x}_q[n]$ denote the output of the system of Fig. 4 with input $u_q[n]$ as in (16). Then we have the following after some algebraic manipulation:

$$\widehat{x}_q[n] = \left[\sum_{k=0}^{M_B-1} h_k e^{-j2\pi f_q d_k}\right] \left(10^{\frac{\mathcal{P}}{20}} e^{j2\pi f_q n}\right)\,. \tag{17}$$

From (17), in order to get $\widehat{x}_q[n] = x_q[n]$ as desired from (16), we need

$$\left[\begin{array}{cccc} e^{-j2\pi f_q d_0} & e^{-j2\pi f_q d_1} & \cdots & e^{-j2\pi f_q d_{M_B-1}} \end{array}\right] \left[\begin{array}{c} h_0 \\ h_1 \\ \vdots \\ h_{M_B-1} \end{array}\right] = 10^{\frac{\mathcal{P}_{\text{out}}[0,q]-\mathcal{P}_{\text{in}}[0]}{20}} e^{j\left(\frac{\pi}{180}\theta[0,q]\right)}\,, \tag{18}$$

satisfied for all q with $0 \le q \le N_f - 1$. If we define the following matrix/vector quantities:

$$[\mathbf{E}]_{k,\ell} \ \triangleq\ e^{-j2\pi f_k d_\ell}\,,\ 0 \le k \le N_f - 1, 0 \le \ell \le M_B - 1\,, \tag{19}$$

$$[\mathbf{h}]_k \ \triangleq\ h_k\,,\ 0 \le k \le M_B - 1\,, \tag{20}$$

$$[\mathbf{g}]_k \ \triangleq\ 10^{\frac{\mathcal{P}_{\text{out}}[0,k]-\mathcal{P}_{\text{in}}[0]}{20}} e^{j\left(\frac{\pi}{180}\theta[0,k]\right)}\,,\ 0 \le k \le N_f - 1\,, \tag{21}$$

then (18) can be compactly expressed in matrix form as follows:

$$\mathbf{E}\mathbf{h} = \mathbf{g}\,. \tag{22}$$

From (19), (20), and (21), note that $\mathbf{E}$ is $N_f \times M_B$, $\mathbf{h}$ is $M_B \times 1$, and $\mathbf{g}$ is $N_f \times 1$. In order to obtain a solution for (22), we must have $M_B \ge N_f$ [21]. For a unique solution here, we will take $M_B = N_f$. In this case, from (19), $\mathbf{E}^{-1}$ exists if and only if all of the delays d_ℓ are distinct and the frequencies f_k are all distinct modulo 1 [21]. As this is the case here, from (22), we have

$$\mathbf{h} = \mathbf{E}^{-1}\mathbf{g}\,, \tag{23}$$

and so the set of linear weights $\{h_k\}_{0\le k\le M_B-1}$ can be found from (20), (23), (19), and (21).

B. Mid Power AM/AM and AM/PM Characteristic Region Modeling

For the mid power region (i.e., $\mathcal{P}_{\text{in}}[0] \le \mathcal{P} \le \mathcal{P}_{\text{in}}[N_P - 1]$), we would like the amplifier model to satisfy the set of AM/AM and AM/PM measurement constraints. From (12) and

(13), this requires choosing the piecewise polynomial coefficients $\widehat{p}_{k,m}(v)$ and $\widehat{\phi}_{k,m}(v)$ to satisfy the following conditions.

Mid power AM/AM and AM/PM characteristic region constraints:
($\mathcal{P}_{\text{in}}[0] \leq \mathcal{P} \leq \mathcal{P}_{\text{in}}[N_P-1]$)

$$\begin{aligned} \text{Input}: \quad & u_{p,q}[n] = 10^{\frac{\mathcal{P}_{\text{in}}[p]}{20}} e^{j2\pi f_q n} \\ \text{Output}: \quad & x_{p,q}[n] = 10^{\frac{\mathcal{P}_{\text{out}}[p,q]}{20}} e^{j\left(2\pi f_q n + \frac{\pi}{180}\theta[p,q]\right)} \end{aligned} \;,\; 0 \leq p \leq N_P-1\,,\; 0 \leq q \leq N_f-1\,. \quad (24)$$

Let $\widehat{x}_{p,q}[n]$ denote the output of the system of Fig. 4 with input $u_{p,q}[n]$ as in (16). Then we have the following after some algebraic manipulation:

$$\widehat{x}_{p,q}[n] = \left[\sum_{k=0}^{M_B-1} 10^{\frac{\widehat{\mathcal{P}}_k(\mathcal{P}_{\text{in}}[p])}{20}} e^{j\left(\frac{\pi}{180}\widehat{\theta}_k(\mathcal{P}_{\text{in}}[p])\right)} e^{-j2\pi f_q d_k}\right] e^{j2\pi f_q n}\,. \quad (25)$$

From (25), in order to get $\widehat{x}_{p,q}[n] = x_{p,q}[n]$ as desired from (24), we need

$$\begin{aligned} &\begin{bmatrix} e^{-j2\pi f_q d_0} & e^{-j2\pi f_q d_1} & \cdots & e^{-j2\pi f_q d_{M_B-1}} \end{bmatrix} \begin{bmatrix} 10^{\frac{\widehat{\mathcal{P}}_0(\mathcal{P}_{\text{in}}[p])}{20}} e^{j\left(\frac{\pi}{180}\widehat{\theta}_0(\mathcal{P}_{\text{in}}[p])\right)} \\ 10^{\frac{\widehat{\mathcal{P}}_1(\mathcal{P}_{\text{in}}[p])}{20}} e^{j\left(\frac{\pi}{180}\widehat{\theta}_1(\mathcal{P}_{\text{in}}[p])\right)} \\ \vdots \\ 10^{\frac{\widehat{\mathcal{P}}_{M_B-1}(\mathcal{P}_{\text{in}}[p])}{20}} e^{j\left(\frac{\pi}{180}\widehat{\theta}_{M_B-1}(\mathcal{P}_{\text{in}}[p])\right)} \end{bmatrix} \\ &\qquad = 10^{\frac{\mathcal{P}_{\text{out}}[p,q]}{20}} e^{j\left(\frac{\pi}{180}\theta[p,q]\right)}\,, \end{aligned} \quad (26)$$

satisfied for all p and q with $0 \leq p \leq N_P-1$ and $0 \leq q \leq N_f-1$. By defining the following vectors:

$$[\mathbf{c}[p]]_k \triangleq 10^{\frac{\widehat{\mathcal{P}}_k(\mathcal{P}_{\text{in}}[p])}{20}} e^{j\left(\frac{\pi}{180}\widehat{\theta}_k(\mathcal{P}_{\text{in}}[p])\right)}\,,\; 0 \leq k \leq M_B-1\,, \quad (27)$$

$$[\mathbf{d}[p]]_k \triangleq 10^{\frac{\mathcal{P}_{\text{out}}[p,k]}{20}} e^{j\left(\frac{\pi}{180}\theta[p,k]\right)}\,,\; 0 \leq k \leq N_f-1\,, \quad (28)$$

it can be shown that (26) can be expressed compactly in matrix form as follows:

$$\mathbf{E}\mathbf{c}[p] = \mathbf{d}[p]\,. \quad (29)$$

Here, $\mathbf{E}$ is the matrix that was defined in (19). Assuming that $M_B = N_f$ and that $\mathbf{E}^{-1}$ exists as above, from (29) we have

$$\mathbf{c}[p] = \mathbf{E}^{-1}\mathbf{d}[p] = \mathbf{f}[p]\,, \quad (30)$$

where $\mathbf{f}[p]$ is an $M_B \times 1$ vector that can be obtained by using (19) and (28). Extracting the k-th component of $\mathbf{c}[p]$ from (27), we have the following from (30):

$$[\mathbf{c}[p]]_k = 10^{\frac{\widehat{\mathcal{P}}_k(\mathcal{P}_{\text{in}}[p])}{20}} e^{j\left(\frac{\pi}{180}\widehat{\theta}_k(\mathcal{P}_{\text{in}}[p])\right)} = [\mathbf{f}[p]]_k\,. \quad (31)$$

From (31), it follows that we must have

$$\begin{aligned} \widehat{\mathcal{P}}_k\left(\mathcal{P}_{\text{in}}[p]\right) &= 20\log_{10}\left(\left|[\mathbf{f}[p]]_k\right|\right)\,, \\ \widehat{\theta}_k\left(\mathcal{P}_{\text{in}}[p]\right) &= \frac{180}{\pi}\arg\left([\mathbf{f}[p]]_k\right)\,. \end{aligned} \quad (32)$$

Recalling (13), it follows that (32) becomes the following:

$$\begin{aligned} \sum_{m=0}^{M_P-1} \widehat{p}_{k,m} \left(\mathcal{P}_{\text{in}}[p]\right) \left(\mathcal{P}_{\text{in}}[p]\right)^m &= 20 \log_{10} \left(\left|[\mathbf{f}[p]]_k\right|\right) , \\ \sum_{m=0}^{M_P-1} \widehat{\phi}_{k,m} \left(\mathcal{P}_{\text{in}}[p]\right) \left(\mathcal{P}_{\text{in}}[p]\right)^m &= \frac{180}{\pi} \arg \left([\mathbf{f}[p]]_k\right) . \end{aligned} \tag{33}$$

Here, (33) must be satisfied for all $0 \leq k \leq M_B - 1$ and $0 \leq p \leq N_P - 1$. From (33), the piecewise polynomial coefficients $\{\widehat{p}_{k,m}(v)\}_{0 \leq m \leq M_P-1}$ and $\left\{\widehat{\phi}_{k,m}(v)\right\}_{0 \leq m \leq M_P-1}$ with knots at $\{\mathcal{P}_{\text{in}}[p]\}_{0 \leq p \leq N_P-1}$ can be obtained for each $0 \leq k \leq M_B - 1$. For example, in MATLAB, the `interp1` function can be used to extract these piecewise polynomial coefficients using (33). In all of the simulations presented in Sec. V, the piecewise polynomials $\left\{\widehat{\mathcal{P}}_k(v)\right\}_{0 \leq k \leq M_B-1}$ and $\left\{\widehat{\theta}_k(v)\right\}_{0 \leq k \leq M_B-1}$ were chosen as *cubic spline interpolants* [16], so that $M_P = 4$ here.

C. High Power Saturation Region Modeling

From the AM/AM and AM/PM measurements of the 50 W 32-way Ka-band SSPA shown in Fig. 7, it can be seen that for large input drive levels, the amplitude appears to saturate, whereas the phase shift appears to grow linearly with drive level. Because of these phenomena, it is worthwhile to see if it is possible to extend this behavior into a high power region above the largest input drive level (i.e., $\mathcal{P} > \mathcal{P}_{\text{in}}[N_P - 1]$). It turns out that using the advance/delay based Wiener model with memoryless nonlinearities as in (12), this is indeed possible for the CW tone inputs that form the basis of the AM/AM and AM/PM measurements.

In order to show this, we must define constraints to be satisfied by the analytical model. For the CW tone inputs forming the basis of the AM/AM and AM/PM measurements, we want the output amplitudes to saturate, whereas we want the output phase shift to increase linearly as a function of the input drive level. Specifically, this leads to the following set of constraints.

High power saturation region constraints: ($\mathcal{P} > \mathcal{P}_{\text{in}}[N_P - 1]$)

$$\begin{aligned} \text{Input}: \quad & u_q[n] = 10^{\frac{\mathcal{P}}{20}} e^{j2\pi f_q n} \\ \text{Output}: \quad & x_q[n] = 10^{\frac{\mathcal{P}_{\text{out}}[N_P-1,q]}{20}} e^{j\left(2\pi f_q n + \frac{\pi}{180}(\alpha_q \mathcal{P} + \beta_q)\right)} \end{aligned} \quad , \ \forall \ \mathcal{P} < \mathcal{P}_{\text{in}}[N_P - 1] \, , \ 0 \leq q \leq N_f - 1 \, . \tag{34}$$

Here, α_q and β_q denote, respectively, the linear and constant coefficients of a linear least squares fit of the AM/PM data for the q-th frequency f_q near the largest input drive level value of $\mathcal{P}_{\text{in}}[N_P - 1]$. It should be noted that $\{\alpha_\ell, \beta_\ell\}_{0 \leq \ell \leq N_f-1}$ is solely a function of the AM/PM characteristics of the amplifier and as such is considered known and given here as it can be precomputed. For example, in MATLAB, these coefficients can be obtained by using the `polyfit` function applied to the AM/PM characteristics.

Let $\widehat{x}_q[n]$ denote the output of the system of Fig. 4 with input $u_q[n]$ as in (34). Then we

have the following after some algebraic manipulation:

$$\widehat{x}_q[n] = \left[\sum_{\ell=0}^{N_f-1} \left(\sum_{k=0}^{M_B-1} K_{k,\ell} e^{-j2\pi f_q d_k} \right) e^{j\left(\frac{\pi}{180}\alpha_\ell \mathcal{P}\right)} \right] e^{j2\pi f_q n} \,. \tag{35}$$

From (35), in order to get $\widehat{x}_q[n] = x_q[n]$ as desired from (34), we need

$$\sum_{\ell=0}^{N_f-1} \left(\sum_{k=0}^{M_B-1} K_{k,\ell} e^{-j2\pi f_q d_k} \right) e^{j\left(\frac{\pi}{180}\alpha_\ell \mathcal{P}\right)} = \left(10^{\frac{\mathcal{P}_{\text{out}}[N_P-1,q]}{20}} e^{j\left(\frac{\pi}{180}\beta_q\right)} \right) e^{j\left(\frac{\pi}{180}\alpha_q \mathcal{P}\right)} \,. \tag{36}$$

A sufficient condition for (36) to be satisfied is the following:

$$\sum_{k=0}^{M_B-1} K_{k,\ell} e^{-j2\pi f_q d_k} = \left(10^{\frac{\mathcal{P}_{\text{out}}[N_P-1,q]}{20}} e^{j\left(\frac{\pi}{180}\beta_q\right)} \right) \delta[\ell - q] \,. \tag{37}$$

Here, $\delta[n]$ denotes the *Kronecker delta function* [6]. For simplicity, define the quantity D_q as follows for $0 \leq q \leq N_f - 1$:

$$D_q \triangleq \left(10^{\frac{\mathcal{P}_{\text{out}}[N_P-1,q]}{20}} e^{j\left(\frac{\pi}{180}\beta_q\right)} \right) \,. \tag{38}$$

Then, from (37) and (38), we have the following:

$$\left[\begin{array}{cccc} e^{-j2\pi f_q d_0} & e^{-j2\pi f_q d_1} & \cdots & e^{-j2\pi f_q d_{M_B-1}} \end{array} \right] \left[\begin{array}{c} K_{0,\ell} \\ K_{1,\ell} \\ \vdots \\ K_{M_B-1,\ell} \end{array} \right] = D_q \delta[\ell - q] \,. \tag{39}$$

Here, (39) must be satisfied for all ℓ and q with $0 \leq \ell, q \leq N_f - 1$. If we define the following matrix quantities:

$$[\mathbf{K}]_{k,\ell} \triangleq K_{k,\ell} \,, \; 0 \leq k \leq M_B - 1, 0 \leq \ell \leq N_f - 1 \,, \tag{40}$$

$$\mathbf{D} \triangleq \text{diag}\left(D_0, D_1, \ldots, D_{N_f-1} \right) \,, \tag{41}$$

then (39) can be expressed compactly in matrix form as follows:

$$\mathbf{EK} = \mathbf{D} \,. \tag{42}$$

As before, $\mathbf{E}$ is the matrix from (19). Assuming that $M_B = N_f$ and that $\mathbf{E}^{-1}$ exists as above, from (42) we have

$$\mathbf{K} = \mathbf{E}^{-1}\mathbf{D} \,, \tag{43}$$

and so the set of high power saturation region coefficients $\{K_{k,\ell}\}_{0 \leq k \leq M_B-1, 0 \leq \ell \leq N_f-1}$ can be found from (40), (43), (19), (41), and (38).

D. Generating a Universal Input Drive Level Axis

The above analysis showed that we could satisfy all of the desired low/mid/high power region constraints through proper choice of the parameters characterizing the analytical

model chosen here. As mentioned previously, the only stipulation was that the AM/AM and AM/PM characteristics be defined over a universal input drive level axis (i.e., over a fixed set of input drive levels for all carrier frequencies). This restriction was enforced in order to allow all of the piecewise polynomials appearing in (12) to share the same knot values (which were the input drive level values themselves).

Though this restriction appears overly constrictive, it turns out that even with it in effect, all of the original AM/AM and AM/PM constraints from (9) can be satisfied. One way to ensure this is to take the universal input drive level axis to be the union of all input drive level values across all carrier frequencies. Specifically, the set of universal input drive level axis values can be generated as follows:

$$\left\{\mathcal{P}_{\text{in}}\left[0\right],\mathcal{P}_{\text{in}}\left[1\right],\ldots,\mathcal{P}_{\text{in}}\left[N_P-1\right]\right\}=\left\{\bigcup_{q=0}^{N_f-1}\bigcup_{p_q=0}^{N_{P_q}-1}P_{\text{in}}\left[p_q,q\right]\right\}. \tag{44}$$

In (44), N_P denotes the number of unique input drive level values among the whole set of given input drive levels and the left hand side elements are assumed to be sorted such that $\mathcal{P}_{\text{in}}\left[0\right]<\mathcal{P}_{\text{in}}\left[1\right]<\cdots<\mathcal{P}_{\text{in}}\left[N_P-1\right]$.

With this kind of universal input drive level axis, a new set of AM/AM and AM/PM measurements from (9) are derived which include the original measurements as a subset. In particular, if there is an input drive level for which there is neither AM/AM nor AM/PM data for a particular frequency, then this data is interpolated (using a spline interpolant [16] for example) using the existing data for that particular frequency. For extrapolation regions (i.e., low and high power regions), we model the amplifier as linear in the low power region as described in Sec. IV-A and saturated in the high power region as described in Sec. IV-C. The set of all such given and interpolated/extrapolated AM/AM and AM/PM measurements then become the sets described in (11).

Though the universal input drive level axis construction method from (44) ensures that all given AM/AM and AM/PM measurements will be satisfied, this may result in an overly large number of piecewise polynomial knots (i.e., N_P), which in turn could become overly computationally complex. Another method to generate a universal input drive level axis which approximates the given AM/AM and AM/PM measurements but is potentially less computationally intensive is to partition the input drive level axis into N_P values uniformly distributed between the smallest and largest given drive levels. This leads to the following universal input drive level axis values:

$$\mathcal{P}_{\text{in}}\left[p\right]=P_{\min}+\left(\Delta P\right)p\,,\;0\leq p\leq N_P-1\,, \tag{45}$$

where we have

$$P_{\min}\triangleq\min_{q,p_q}\left\{P_{\text{in}}\left[p_q,q\right]\right\}\;,\;P_{\max}\triangleq\max_{q,p_q}\left\{P_{\text{in}}\left[p_q,q\right]\right\}\;,\;\Delta P\triangleq\frac{P_{\max}-P_{\min}}{N_P-1}\,.$$

As was done previously above, a new set of AM/AM and AM/PM measurements is constructed for this universal input drive level axis by interpolation/extrapolation from the given AM/AM and AM/PM data to obtain the sets described in (11). It should be

stressed that, in general, the given AM/AM and AM/PM measurements will only be approximately satisfied by the analytical model considered here. However, for many practical simulation scenarios, such as those considered in Sec. V, this approximation is quite good and can offer a dramatic reduction in computational complexity as compared with the universal input drive level axis construction method of (44).

For sake of notational convenience, we will refer to the universal input level axis construction approach of (44) as the *union* method and that of (45) as the *uniform* method.

V. Simulation Results for the Piecewise Polynomial Wiener Model

In this section, we present simulation results for the advance/delay based Wiener system with piecewise polynomial type nonlinearities. The amplifier data used to construct this wideband model was the 50 W 32-way Ka-band SSPA. As will soon be shown, there are notable differences between the results obtained for wideband and narrowband input signals. For all of the simulations presented here, each wideband input signal had a bandwidth 500 MHz (i.e., F_{BW} from Sec. III was 500 MHz), whereas each narrowband input signal had a bandwidth of at most 50 MHz.

A. Noise Power Ratio (NPR) Results

One common way to gauge the linearity of an amplifier is to calculate the *noise power ratio* (NPR) figure [22], which measures the amount of spectral leakage placed in a notch of a multi-tonal input to the amplifier. Specifically, the input to the amplifier is a frequency rich multi-tonal signal with a power spectral density (PSD) as shown in Fig. 9(a). Here, the PSD is spectrally flat over the band of interest, except for a notch placed at the carrier frequency. Typically, the notch depth is designed to be large and on the order of 50 dB [22]. Nonlinearities present in the amplifier will tend to place harmonic content within the notch, as shown by the output PSD from Fig. 9(b). The NPR measures the amount of leakage induced by the amplifier in the notch region. Specifically, it is a ratio between the output PSD level in the region of harmonic interest and the same level in the notch region. A larger NPR implies a higher degree of amplifier linearity [22]. Typically, an amplifier is considered relatively linear for NPR values in excess of 25 dB.

In Fig. 10, we have plotted the NPR as a function of input drive level for (a) the wideband case and (b) the narrowband case. For both cases, a contour plot corresponding to an NPR value of 25 dB has been overlaid on the images. As can be seen here, the results for both the wideband and narrowband cases are similar, although there is more erratic behavior of the NPR for the wideband case. One of the reasons for this is that the frequency selective nature of the wideband amplifier in this case may make the NPR measure as defined in Fig. 9 require more averaging than for the narrowband case. Another observation that can be made from Fig. 10 is that the amplifier appears to be more linear for carrier frequencies in the range 33-34 GHz and less so for carrier

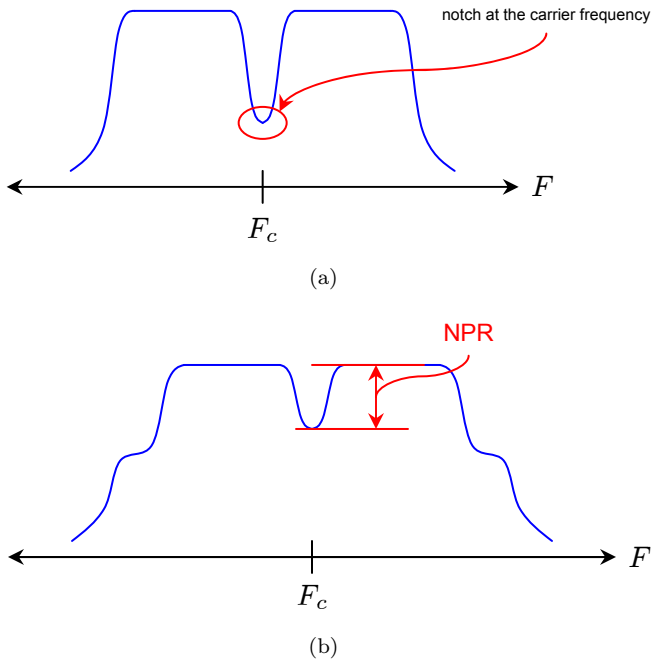

Figure 9. Noise power ratio (NPR) setup: (a) notched multi-tone input PSD and (b) amplifier distorted output PSD.

frequencies in the range 30-31 GHz. This appears to be consistent with the behavior of the AM/PM measurements as shown in Fig. 6(b).

Image plots of the output power as a function of input drive level for an NPR type input signal as in Fig. 9 are shown in Fig. 11 for (a) the wideband case and (b) the narrowband case. Though both plots appear similar, it can be seen that the plot for the wideband case appears smoother than for the narrowband input setting. This is an artifact of the gradual transitioning of the bandwidth as the carrier frequency is swept for the wideband case, which does not occur for the narrowband case. A careful inspection between Fig. 11 and Fig. 6(a) suggests that the output power for the NPR type input signal behaves approximately the same as the CW tones characterizing the AM/AM and AM/PM measurements.

In Fig. 12, image plots of the NPR as a function of output power are shown for (a) the wideband case and (b) the narrowband case. Overlaid across both plots are two curves: one in a black corresponding to the NPR = 25 dB contour and another in red corresponding to the 1 dB compression point output power [4] (i.e., the output power corresponding to a gain compression of 1 dB). A careful inspection of Fig. 12(a) and (b) suggests that the amplifier appears to be able to operate more linearly for a slightly larger range of output powers for the narrowband case than for the wideband case. For example, at an output power of 35 dBm, it can be seen that on average, the NPR appears to be slightly larger for the narrowband case than for the wideband case. In addition to this, it can be seen from the plots that the curve corresponding to the 1 dB compression point

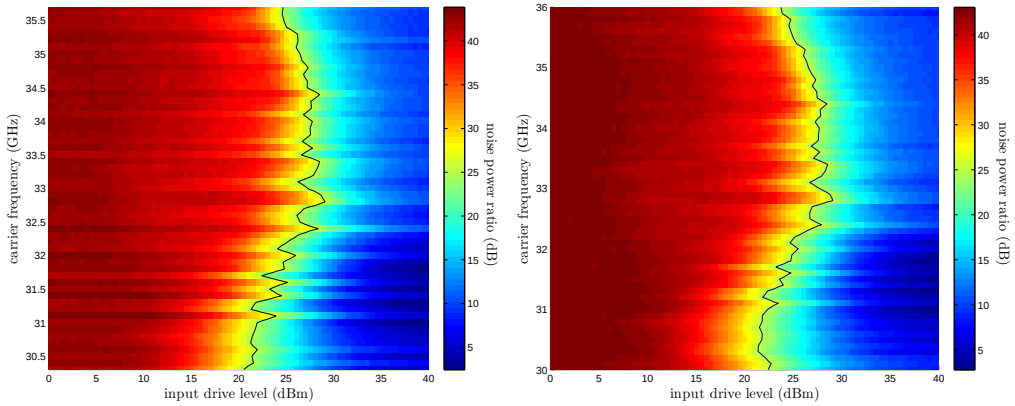

Figure 10. Image plots of NPR as a function of input drive level: (a) wideband case and (b) narrowband case. (Images overlaid with an NPR = 25 dB contour plotted in black.)

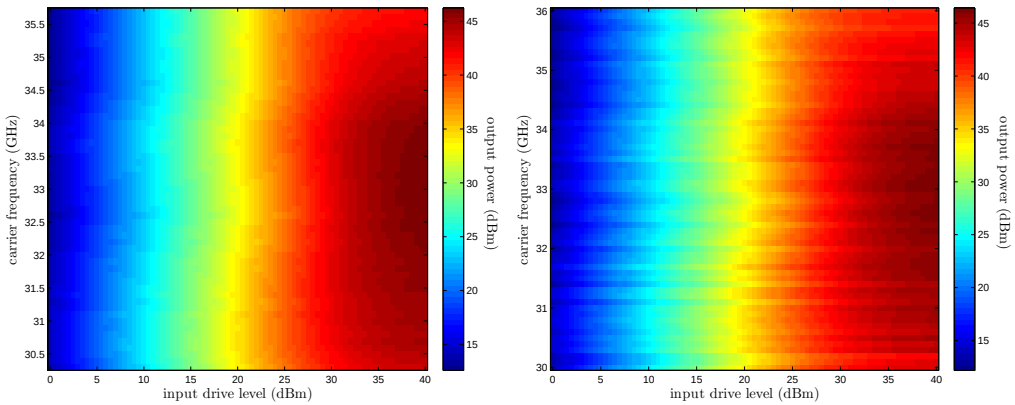

Figure 11. Image plots of output power as a function of input drive level for an NPR type input signal: (a) wideband case and (b) narrowband case.

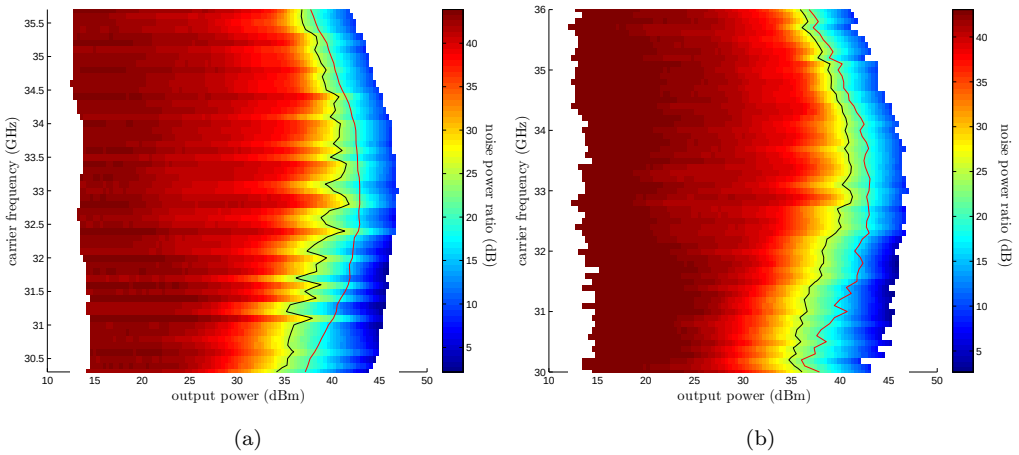

Figure 12. Image plots of NPR as a function of output power: (a) wideband case and (b) narrowband case. (Images overlaid with an NPR = 25 dB contour plotted in black and the 1 dB compression point reference power curve in red.)

output power is smoother for the wideband case than for the narrowband case. As discussed earlier, the reason for this can be traced to the gradual transitioning of the bandwidth as the carrier frequency is varied for the wideband case.

Finally, in Fig. 13, we have plotted the NPR as a function of the output back-off (OBO) [4] for (a) the wideband case and (b) the narrowband case. As before, the plots have been overlaid with a contour corresponding to NPR = 25 dB. Here, the OBO is defined with respect to the 1 dB compression point output power. Specifically, if P_{out} denotes the output power and $P_{\text{out;1 dB}}$ denotes the output power corresponding to the 1 dB compression point, the OBO is defined as follows here [4]:

$$\text{OBO} \triangleq \frac{P_{\text{out;1 dB}}}{P_{\text{out}}}\,.$$

As can be seen from Fig. 13, more back-off appears to be required to obtain a satisfactory NPR for the wideband case than for the narrowband case. This is in line with the intuition that the additional frequency selectivity seen by the wideband input signal as compared with the narrowband input will result in more degradation from the amplifier.

B. Telemetry Waveform Sample Density and Spectral Regrowth Results

One intuitive way to better understand the effects a nonlinear amplifier has on an input signal is to view the warping of the signal waveform in the time domain. For telemetry signals, this can be viewed by looking at the distribution of the CB waveform samples in the in-phase (I) and quadrature (Q) plane [5]. When viewed in the I/Q-plane, these signals bear resemblance to the data symbol constellations from which they are derived, but include additional values due to pulse shaping and symbol transitions.

As an example, suppose that the input to the 50 W 32-way Ka-band SSPA is a 16-symbol

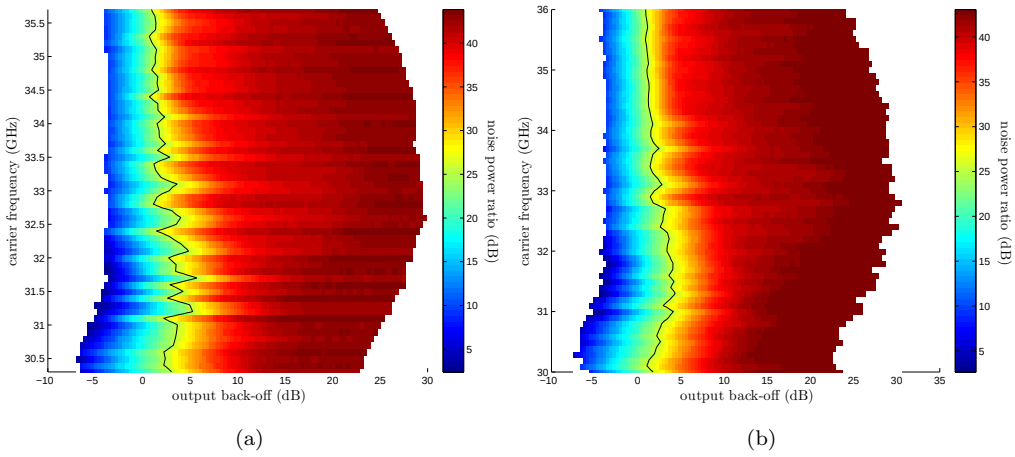

Figure 13. Image plots of NPR as a function of OBO: (a) wideband case and (b) narrowband case. (Images overlaid with an NPR = 25 dB contour plotted in black.)

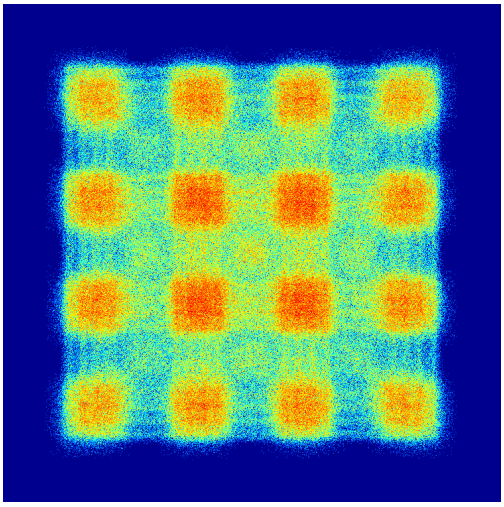

Figure 14. CB sample density plot of an ideal 16-QAM, 0.5 roll-off SRRC telemetry signal.

quadrature amplitude modulation (QAM) [5] (i.e., 16-QAM) type telemetry signal shaped by a square-root raised cosine (SRRC) pulse [5] with a roll-off factor of 0.5. In this case, a plot of the density of the samples prior to amplification is as shown in Fig. 14. Here, as the color ranges from blue to red, the sample density increases logarithmically. As can be seen in Fig. 14, the most frequent samples occur near the 16-QAM constellation point values. The clustering of points in these and other regions is the result of the pulse shaping used here as well as symbol transitions.

Suppose this ideal 16-QAM, 0.5 roll-off SRRC telemetry signal is input to the 32-way SSPA model with an input drive level of 25 dBm at a carrier frequency of 31.3 GHz (corresponding to the most dynamic AM/PM characteristic as seen from Fig. 6(b)). Then, the resulting sample density plots are shown in Fig. 15 for (a) a wideband (i.e., 500 MHz

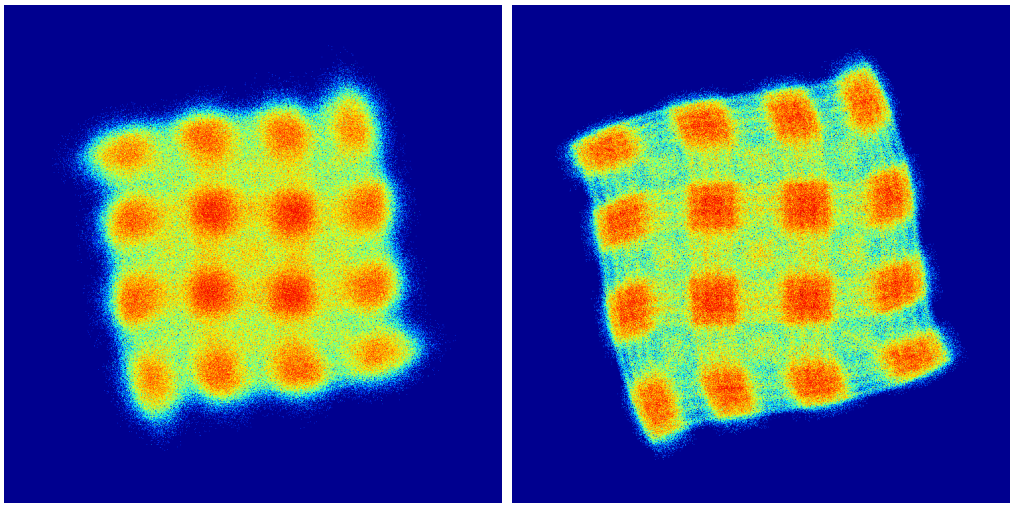

(a) (b)

Figure 15. CB sample density plots for an amplified 16-QAM, 0.5 roll-off SRRC telemetry signal: (a) wideband input (500 MHz bandwidth) and (b) narrowband input (5 MHz bandwidth).

bandwidth) signal and (b) a narrowband signal (with a bandwidth of 5 MHz). As can be seen, for both inputs, the points corresponding to the outermost constellation symbols are distorted the most as they correspond to a larger power than the inner symbols. Furthermore, the warping in these regions is clearly observed to be a combination of both AM and PM distortion.

One interesting difference between the wideband and narrowband results of Fig. 15 is that the wideband density appears to be more smeared than the narrowband density. This smearing is attributed to the frequency selectivity present for the wideband case. As will be shown subsequently in Sec. V-D, the result of this is a deleterious effect on the bit error rate (BER), in line with intuition.

In addition to viewing the density of the temporal samples of the amplifier output, it is also insightful to consider a frequency domain interpretation of the results. This can be achieved by considering the PSDs of the amplifier outputs. In Fig. 16, we have plotted the amplifier model output PSDs for (a) the 500 MHz wideband input and (b) the 5 MHz narrowband input.

From this figure, several interesting observations can be made. First of all, both the wideband and narrowband outputs include a significant amount of *spectral regrowth* [4, 22] (i.e., harmonic content generated outside the bandwidth of interest). One difference between these two cases, however, is that the spectral regrowth is asymmetric for the wideband output but symmetric for the narrowband output. Intuitively, this makes sense since the wideband signal will see frequency selective aspects of the amplifier that the narrowband signal will not. Furthermore, it can be seen that the spectral regrowth for the wideband case extends over a proportionally wider range than for the narrowband case.

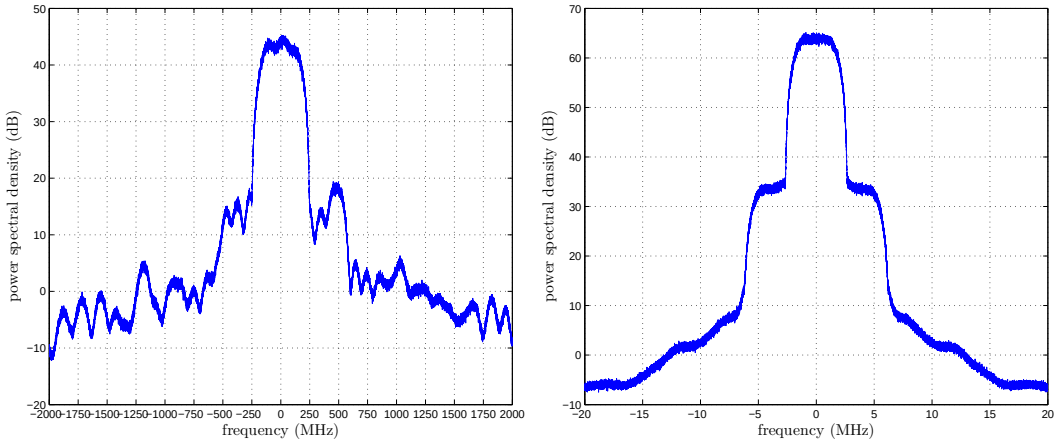

(a) (b)

Figure 16. PSD plots for an amplified 16-QAM, 0.5 roll-off SRRC telemetry signal: (a) wideband input (500 MHz bandwidth) and (b) narrowband input (5 MHz bandwidth).)

This is also in line with the intuition that the amplifier will distort a wideband signal in a more deleterious manner than a narrowband one.

Another way in which the differences between the wideband and narrowband cases manifest is in terms of output power. For the wideband signal, the output power was observed to be 38.76 dBm, whereas for the narrowband signal, the output power was found to be 39.35 dBm. This difference in output power is not significant, but is in line with intuition here.

C. Error Vector Magnitude (EVM) and Out-of-Band Power Results

To help gauge the amplifier distortion effects on a telemetry input signal, we will focus on two types of metrics here. The first measures the effect that the amplifier nonlinearities have on demodulation, whereas the second quantitatively measures the spectral regrowth induced on the transmitted telemetry signal.

To introduce the first metric, known as the error vector magnitude (EVM) [23], recall the distorted telemetry signals of Sec. V-B. If these signals are respectively received and processed through an ideal *matched filter* [5], the resulting output will not exactly lie on the original constellation lattice points but will instead by displaced from them. (Implicitly we assume that the received soft symbol stream has been optimally scaled and rotated to match the original constellation via an automatic gain control (AGC) [5] and phase locked loop (PLL) [5], respectively.) For example, if $d[n]$ denotes the original transmitted symbol stream, then we will obtain $\widehat{d}[n]$, which will in general be displaced from $d[n]$ by some amount $\epsilon[n] \triangleq d[n] - \widehat{d}[n]$. This is illustrated in the I/Q-plane in Fig. 17.

From Fig. 17, the EVM is defined as the magnitude of the *error vector* $\{\epsilon[n]\}$ normalized

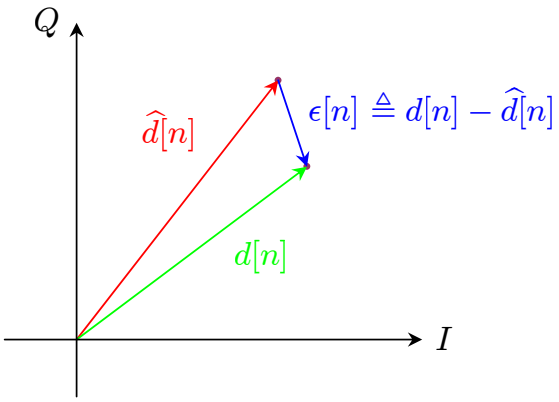

Figure 17. Illustration of the error vector between a desired and actual point in the I/Q-plane.

by the magnitude of the *desired vector* $\{d[n]\}$ [23]. Mathematically, the EVM is defined as follows [23]:

$$\text{EVM} \triangleq \sqrt{\frac{\sum\limits_{n} |\epsilon[n]|^2}{\sum\limits_{n} |d[n]|^2}} = \sqrt{\frac{\sum\limits_{n} \left|d[n] - \widehat{d}[n]\right|^2}{\sum\limits_{n} |d[n]|^2}}\,.$$

Typically, the EVM is reported in terms of percentage [23].

The second metric we will consider here is the out-of-band power [5], which quantitatively measures the spectral regrowth present in the output signal. If $S_{x_{\text{CB}}}\left(e^{j2\pi f}\right)$ denotes the PSD of the amplifier output signal [6, 7], then the out-of-band power is simply the ratio of the out-of-band spectral content to the total power. Mathematically, it is defined as follows [5]:

$$\text{out-of-band power} \triangleq \frac{\displaystyle\int_{-\frac{1}{2}}^{\frac{1}{2}} S_{x_{\text{CB}}}\left(e^{j2\pi f}\right)\, df - \int_{-\frac{f_{\text{BW}}}{2}}^{\frac{f_{\text{BW}}}{2}} S_{x_{\text{CB}}}\left(e^{j2\pi f}\right)\, df}{\displaystyle\int_{-\frac{1}{2}}^{\frac{1}{2}} S_{x_{\text{CB}}}\left(e^{j2\pi f}\right)\, df}\,.$$

Here, we will report the out-of-band power in dB.

Returning to the simulations, in Figs. 18 and 19, we have plotted the EVM and out-of-band power, respectively, for (a) a wideband input signal and (b) a narrowband input. Here, the input was chosen to be a 16-QAM, 0.5 roll-off SRRC shaped telemetry signal, as was done previously in Sec. V-B.

As can be seen from Fig. 18, the EVM appears to be related to the AM/PM characteristics of the amplifier (see Fig. 6(b)). One notable difference between the wideband and narrowband cases is that the EVM is notably larger for the wideband case. This is due to the frequency selectivity incurred for the wideband case that is not present in the narrowband case.

From Fig. 19, it can be seen that the out-of-band power is noticeably larger for the

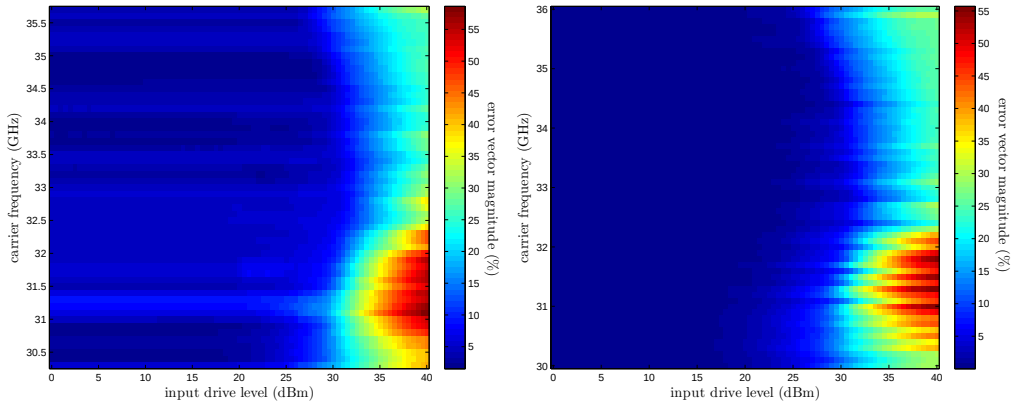

(a) (b)

Figure 18. Image plots of EVM as a function of input drive level: (a) wideband case and (b) narrowband case.

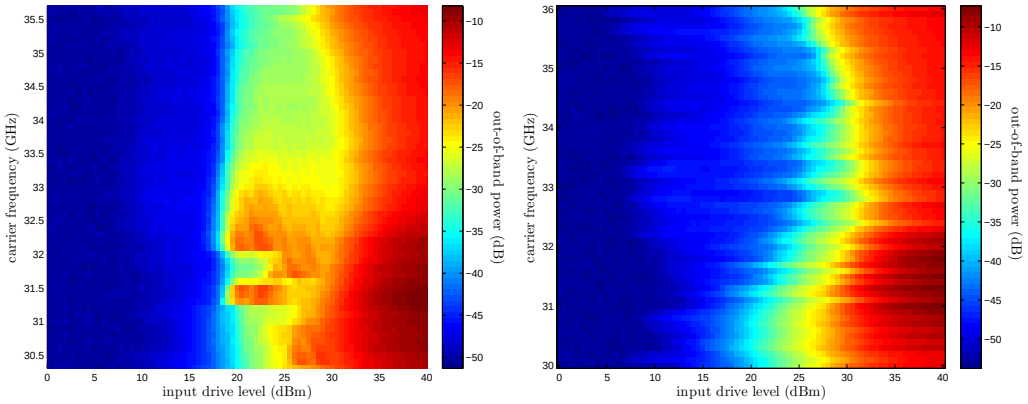

(a) (b)

Figure 19. Image plots of out-of-band power as a function of input drive level: (a) wideband case and (b) narrowband case.

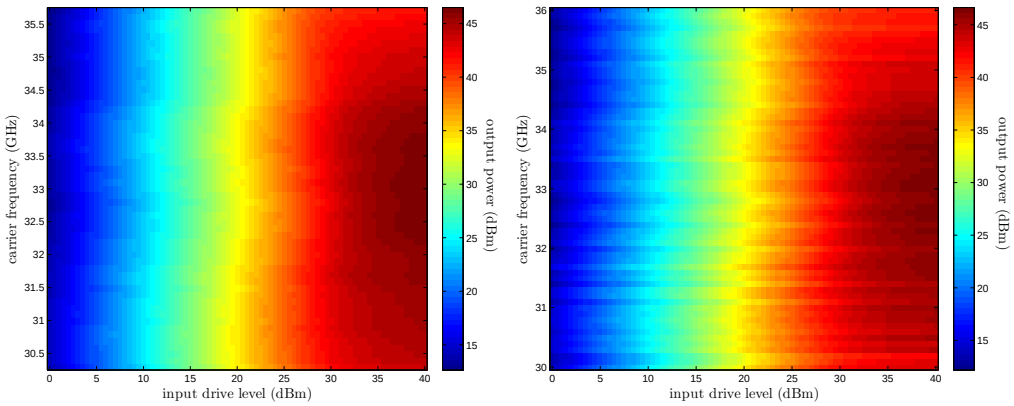

Figure 20. Image plots of output power as a function of input drive level for a 16-QAM, 0.5 roll-off SRRC type telemetry input signal: (a) wideband case and (b) narrowband case.

wideband case at moderate input drive levels. This is attributed to the presence of a spurious spectral component located at 31.3 GHz at RF (which corresponds to the most dynamic of the AM/AM and AM/PM characteristics). Specifically, for the wideband input signal case, the amplifier model induces a nonlinear coupling resulting in this spurious harmonic content. On the other hand, for the narrowband case, such nonlinear harmonic coupling is not present.

In Fig. 20, we have plotted the output power as a function of the input drive level for the telemetry input signal. Comparing Figs. 20 and 11, it is evident that both the NPR and telemetry inputs yield the similar types of input drive level/output power relations.

In Figs. 21 and 22, the EVM and out-of-band power have been plotted as a function of the output power, respectively. As with the NPR results, we have included plots of the 1 dB compression point reference power. From the figures, it is clear that the 1 dB compression point curve is smoother for the wideband case than the narrowband one, as was the case for the NPR input signal scenario.

Finally, in Figs. 23 and 24, we have plotted the EVM and out-of-band power as a function of the OBO, respectively. From these figures and results in general, the similarities and differences between the amplifier effects for wideband and narrowband inputs become apparent.

D. Bit Error Rate (BER) Results

An important figure of merit to measure the degradations caused by an amplifier is the bit error rate (BER) [5], which is typically computed as a function of the bit signal-to-noise ratio (SNR) [5]. In Fig. 25, we have plotted the BERs obtained for both the wideband and narrowband cases for a variety of OBO levels. The telemetry signal considered was a

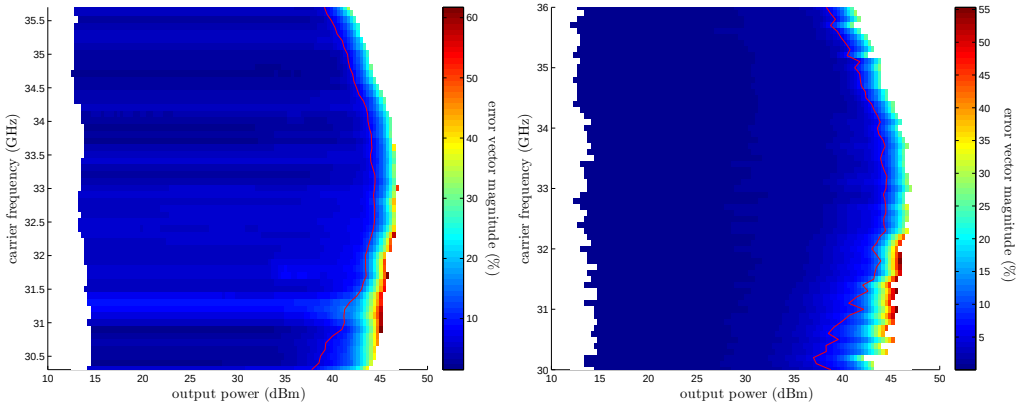

Figure 21. Image plots of EVM as a function of output power: (a) wideband case and (b) narrowband case. (Images overlaid with the 1 dB compression point reference power curve plotted in red.)

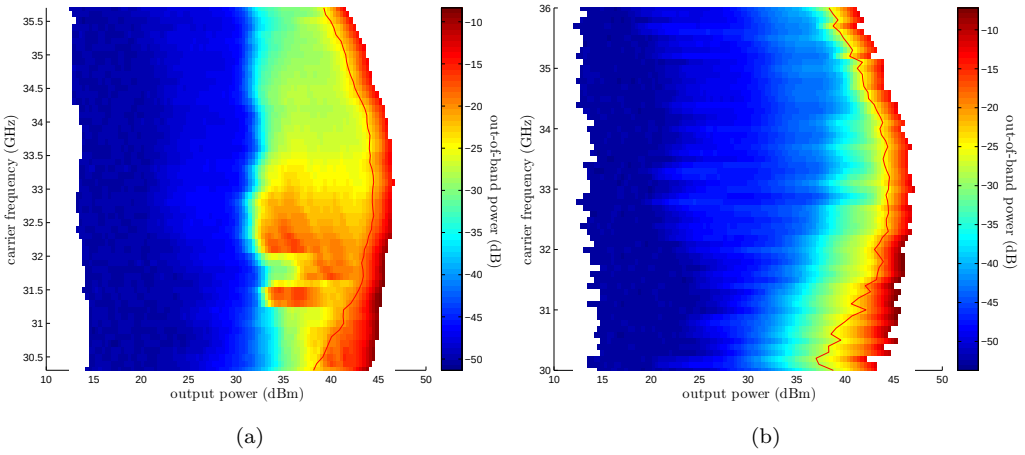

Figure 22. Image plots of out-of-band power as a function of output power: (a) wideband case and (b) narrowband case. (Images overlaid with the 1 dB compression point reference power curve plotted in red.)

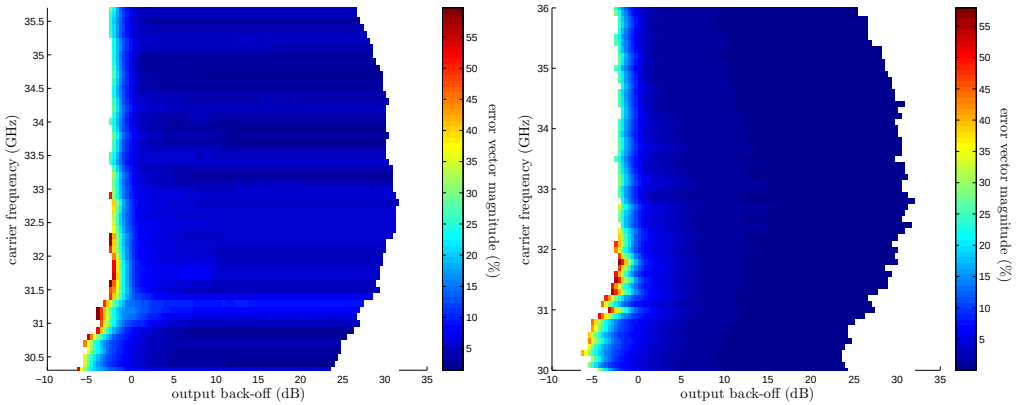

(a) (b)

Figure 23. Image plots of EVM as a function of OBO: (a) wideband case and (b) narrowband case.

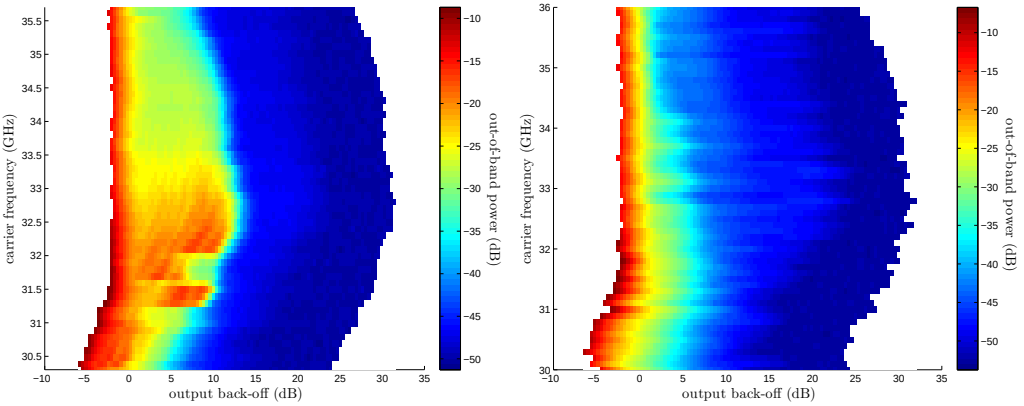

(a) (b)

Figure 24. Image plots of out-of-band power as a function of OBO: (a) wideband case and (b) narrowband case.

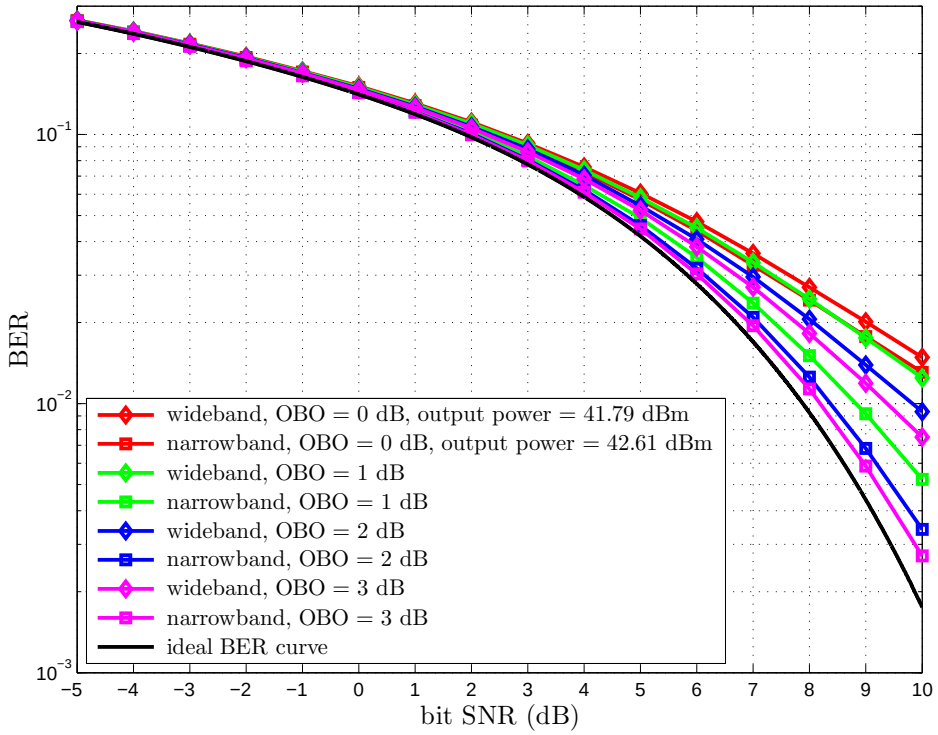

Figure 25. Various BER curves for a 16-QAM, 0.5 roll-off SRRC telemetry signal at carrier frequency 31.3 GHz.

16-QAM, 0.5 roll-off SRRC input at a carrier frequency of 31.3 GHz. In addition to the empirical curves obtained using the data from the amplifier model, we have also included the ideal BER for 16-QAM [5] for comparison.

From Fig. 25, several interesting observations can be made. First of all, it can be seen that in all cases considered, for a fixed OBO, the BER for the narrowband signal was lower than for the wideband one. This is in line with intuition here. In addition, it can be seen that the empirical BERs approached the ideal BER as the OBO increased. This behavior is as expected, since the amplifier will behave more linearly as the back-off is increased. Finally, note that the bit SNR gap between the theoretical BER and the empirical wideband BER can be in excess of 2 dB. This brings to light the deleterious effects of the amplifier for wideband input signals.

VI. Concluding Remarks

In this article, we proposed an advance/delay based Wiener system with piecewise polynomial type memoryless nonlinearities as a complex baseband model for a nonlinear power amplifier. We showed how to construct such a system to exactly accommodate any desired set of given carrier frequency dependent AM/AM and AM/PM characteristics. Simulation results provided here elucidated the additional deleterious effects due to

frequency selectivity for wideband input signals as opposed to narrowband inputs.

Though the simulation results for the 50 W 32-way Ka-band SSPA appear intuitively correct, to truly validate the proposed Wiener model, it is necessary to substantiate it using actual typical data (such as telemetry data, for example). Once model validation has been established, a worthwhile next step would be the design of a complex baseband digital predistortion system [4, 24] to linearize the amplifier as best as possible. As the dual of a Wiener nonlinear system is a Hammerstein type structure, the most likely candidate for a digital predistortion model in this setting would be a Hammerstein nonlinear system. Investigation of such systems for digital predistortion is the subject of future research.

References

[1] A. Hernandez, S. Haque, H. Endler, J. Ocampo, and D. J. Bell, "High-rate Ka-band TX/RX link demonstrations and characterizations," Research & Technology Development: Annual Report, Jet Propulsion Laboratory, Tech. Rep., 2008.

[2] L. W. Epp, S. Haque, and A. Hernandez, "High-rate Ka-band TX/RX link demonstrations and characterizations," Research & Technology Development: Annual Report, Jet Propulsion Laboratory, Tech. Rep., 2009.

[3] S. Haque, L. W. Epp, and S. Li, "High-rate Ka-band TX/RX link demonstrations and characterizations," Research & Technology Development: Annual Report, Jet Propulsion Laboratory, Tech. Rep., 2010.

[4] M. C. Jeruchim, P. Balaban, and K. S. Shanmugan, *Simulation of Communications Systems: Modeling, Methodology, and Techniques*, 2nd ed. New York, NY: Kluwer Academic/Plenum Publishers, 2000.

[5] M. K. Simon, S. M. Hinedi, and W. C. Lindsey, *Digital Communications Techniques: Signal Design and Detection*. Upper Saddle River, NJ: Prentice Hall PTR, 1994.

[6] A. V. Oppenheim and R. W. Schafer, *Discrete-Time Signal Processing*, 3rd ed. Upper Saddle River, NJ: Prentice-Hall, Inc., 2009.

[7] P. P. Vaidyanathan, *Multirate Systems and Filter Banks*. Englewood Cliffs, NJ: Prentice Hall PTR, 1993.

[8] H. Ku, M. D. McKinley, and J. S. Kenney, "Quantifying memory effects in RF power amplifiers," *IEEE Trans. Microw. Theory Tech.*, vol. 50, no. 12, pp. 2843–2849, Dec. 2002.

[9] H. Ku and J. S. Kenney, "Behavioral modeling of nonlinear RF power amplifiers considering memory effects," *IEEE Trans. Microw. Theory Tech.*, vol. 51, no. 12, pp. 2495–2504, Dec. 2003.

[10] N. Safari, P. Fedorenko, J. S. Kenney, and T. Røste, "Spline-based model for digital predistortion of wide-band signals for high power amplifier linearization," in *Proc.*

IEEE MTT-S International Microwave Symposium (IMS 2007), Honolulu, Hawaii, USA, Jun. 3–8, 2007, pp. 1441–1444.

[11] Y. Ye, T. Liu, X. Zeng, and J. He, "Generalized Hammerstein-based dynamic nonlinear behavior models for wideband RF transmitters," in *Proc. International Conference on Wireless Communications, Networking and Mobile Computing (WiCOM 2007)*, Shanghai, China, Sep. 21–25, 2007, pp. 684–687.

[12] A. A. M. Saleh, "Frequency-independent and frequency-dependent nonlinear models of TWT amplifiers," *IEEE Trans. Commun.*, vol. COM-29, no. 11, pp. 1715–1720, Nov. 1981.

[13] C. P. Silva, C. J. Clark, A. A. Moulthrop, and M. S. Muha, "Optimal-filter approach for nonlinear power amplifier modeling and equalization," in *Proc. IEEE MTT-S International Microwave Symposium (IMS 2000)*, vol. 1, Boston, Massachusetts, USA, Jun. 11–16, 2000, pp. 437–440.

[14] C. J. Clark, C. P. Silva, A. A. Moulthrop, and M. S. Muha, "Power-amplifier characterization using a two-tone measurement technique," *IEEE Trans. Microw. Theory Tech.*, vol. 50, no. 6, pp. 1590–1602, Jun. 2002.

[15] P. Singerl and G. Kubin, "Constructing memory-polynomial models from frequency-dependent AM/AM and AM/PM measurements," in *Proc. IEEE International Midwest Symposium on Circuits and Systems (MWSCAS 2007)*, Montréal, Canada, Aug. 5–8, 2007, pp. 321–324.

[16] I. J. Schoenberg, *Cardinal Spline Interpolation*, ser. CBMS-NSF Regional Conference Series in Applied Mathematics. Philadelphia, PA: Society for Industrial and Applied Mathematics, 1973, no. 12.

[17] C. Peng, W. Jiang, Y. Ni, J. Wang, X. Yu, B. Xing, and X. Zhu, "Modeling of nonlinear power amplifier with memory effects applied for 3G system," in *Proc. Asia-Pacific Microwave Conference (APMC 2005)*, vol. 2, Suzhou, China, Dec. 4–7, 2005, pp. 1–3.

[18] P. Alper, "A consideration of the discrete Volterra series," *IEEE Trans. Autom. Control*, vol. 10, no. 3, pp. 322–327, Jul. 1965.

[19] A. Zhu and T. J. Brazil, "RF power amplifier behavioral modeling using Volterra expansion with Laguerre functions," in *Proc. IEEE MTT-S International Microwave Symposium Digest, 2005*, Long Beach, California, USA, Jun. 12–17, 2005, pp. 1–4.

[20] ——, "Behavioral modeling of RF power amplifiers based on pruned Volterra series," *IEEE Microw. Wireless Compon. Lett.*, vol. 14, no. 12, pp. 563–565, Dec. 2004.

[21] R. A. Horn and C. R. Johnson, *Matrix Analysis*. Cambridge, UK: Cambridge University Press, 1985.

[22] A. Geens, Y. Rolain, W. V. Moer, K. Vanhoenacker, and J. Schoukens, "Discussion on fundamental issues of NPR measurements," *IEEE Trans. Instrum. Meas.*, vol. 52, no. 1, pp. 197–202, Feb. 2003.

[23] K. M. Gharaibeh, K. G. Gard, and M. B. Steer, "Accurate estimation of digital communication system metrics - SNR, EVM and ρ in a nonlinear amplifier environment," in *Proc. 64th Automatic RF Techniques Group (ARFTG) Microwave Measurement Conference*, Orlando, Florida, USA, Nov. 30–Dec. 3, 2004, pp. 41–44.

[24] N. Safari, N. Holte, and T. Røste, "Digital predistortion of power amplifiers based on spline approximations of the amplifier characteristics," in *Proc. IEEE Vehicular Technology Conference (VTC2007-Fall)*, Baltimore, Maryland, USA, Sep. 30–Oct. 3, 2007, pp. 2075–2080.